# Influence of rare earth substitution on structure, photoluminescence emission properties and Judd-Ofelt analysis of ZnS:Eu$^{3+}$ red phosphors

L.S. Archana [a,*], Deepthi N. Rajendran [a], Jincemon Cyriac [b,c,d]

[a] Department of Physics, Govt.College for Women, University of Kerala, Thiruananthapuram, Kerala, 695014, India
[b] Department of Physics, St. Thomas College, Arunapuram, Palai, Kottayam, Kerala, 686574, India
[c] Department of Physics, Deva Matha College, Kuravilangad, Kottayam, Kerala, 686633, India
[d] PG Department of Physics, Sree Narayana College, Chengannur, Alappuzha, Kerala, 689508, India

## ABSTRACT

A series of Eu$^{3+}$ doped ZnS red emitting phosphors were synthesized by conventional low temperature solid state reaction technique. The structural and spectroscopic characteristics of the prepared materials were examined by theoretical and experimental methods. The XRD results confirm the formation of hexagonal structured ZnS material. Similar morphology is obtained from TEM and SEM analysis and the particle size and grain size were calculated. The compositional analysis using EDS confirms the atomic percentage present in the materials. The optical band gap energy of the samples varied from 3.59 to 3.43 eV. The PL emission under excitation 390 nm has greater emission intensity at concentration $x = 0.1$ in $Zn_{(1-x)}S: xEu^{3+}$ material. The intense red emission (614 nm) for concentration $x = 0.1$ have CIE coordinates (0.6090, 0.3905) with color purity 90.41% and CCT 1629.26 K. The site symmetry of Eu$^{3+}$ ions was explained using PL emission spectra. The intensity parameters $\Omega_2$, $\Omega_4$ and $\Omega_6$, radiative properties like branching ratio ($\beta_R$), transition radiative parameter ($A_R$), stimulated emission cross section $\sigma_e$, radiative life time ($\tau_R$) was calculated from Judd-Ofelt theory. The luminescence decay kinetics was analyzed and the life time of material was calculated in millisecond (ms) range. The strong and intense red emission and the improved stimulated emission cross section offer Eu$^{3+}$ doped ZnS material useful for designing optoelectronic device applications.

## 1. Introduction

The major challenges affecting the global community include energy conservation and environmental management. Active research is going on in materials science to develop environmental friendly high performance devices with good efficiency [1]. Researchers are interested in the development of semiconductor nanophosphors because of their size-dependent optical properties [2]. These size reduced phosphor materials can be tuned to their properties for applications in optoelectronic devices. The unique luminescence characteristics of nanophosphor sulphide semiconductor materials can be changed by reducing dimensions and tuning the band gap [3]. The surface imperfections of nanophosphor particles illustrate their excellent optical properties. This is due to the recombination of excitons on the surface of nanophosphors [4]. The small size of nanophosphors material coated in LED surface offer a solution for saving the energy as well as the material [5].

Compared to other II-VI group semiconductor materials, ZnS is the most suitable host material for rare earth doping because it has better chemical stability with a wider direct band gap energy (Eg = 3.67 eV) at room temperature. It is used as a phosphor material in electroluminescent (EL) devices, Light emitting diodes (LEDs), p-type conductors, field emitters, solar cells, flat panel displays, IR windows, sensors, photo catalysis, lasers, nanogenerators etc. [6]. Therefore, ZnS was chosen as the host material for doping to enhance its optical properties. Under ambient conditions, ZnS exists in two phases: Sphalerite (Cubic) with lattice parameters $a = b = c = 5.41$ Å, Space group $F\overline{4} - 3m$ and Wurtzite (Hexagonal) with that of $a = b = 3.82$ Å, $c = 6.26$ Å, Space group $= P6_3mc$ [7]. This small difference in the arrangement of the atoms creates large differences in the band structures and the optical properties of the systems. The hexagonal phase shows better optical properties than the cubic phase [8]. The hexagonal ZnS has a stronger blue emission than cubic ZnS, which is the thermally unstable phase. This may be due to the distribution of Zn$^{2+}$ ions and the interatomic distance between them, since hexagonal is much closer than the cubic.

---

* Corresponding author.
E-mail address: archana0133@gmail.com (L.S. Archana).

This difference in the atomic arrangements affects the luminescence properties. The site symmetry of cubic and hexagonal is quite different [9]. The synthesis of hexagonal phase of ZnS is a major challenge to researchers, since it converts to cubic phase under room temperature conditions [10]. In ZnS nanophosphors, the electrons are excited from the ZnS valance band to the conduction band by absorbing energy equal to or greater than the band gap energy. These excited electrons relaxed to some surface states give luminescence in the visible region [11]. ZnS has lower intensity luminescence in the short wave region of the visible region and this can be improved by doping ions having their own emitting transitions. The dopant ion occupies the Zn lattice site and acts as a trap centers for electrons and holes after doping [12]. ZnS doped with optically active luminescence centers, designs advanced break for luminescent materials by changing the band structure of the nano-material. The doping affects the range of emission spectra and luminescence efficiency, which greatly influences the practical applications [13]. $Eu^{3+}$ is the most studied lanthanide ion due to its relatively high stability and the low reduction potential ($Eu^{3+} = 0.35$ V). $Eu^{3+}$ doped ZnS is important because of its high brightness and tunable emission wavelength from blue to red, have technological and industrial applications [14]. Though the synthesis of $Eu^{3+}$ doped ZnS is a challenging work, many researchers have studied the $Eu^{3+}$ doped ZnS because of the low phonon energy of ZnS and the energy transfer between ZnS and $Eu^{3+}$ ion center are quite astonishing. The incorporation of $Eu^{3+}$ into ZnS materials will yield new opportunities to displays, optoelectronic devices, LEDs, sensors, mobile phones etc [15]. The incorporation of $Eu^{3+}$ into ZnS lattice, which is very difficult due to large difference in ionic radii, can be made possible by choosing proper synthesis method [16]. Moreover, $Eu^{3+}$ ions are considered as sensitive structure probes to explain the local site symmetry. When $Eu^{3+}$ ion is doped in to ZnS host material, the luminescent properties of $Eu^{3+}$ ions depend on their site symmetry. The difference in the site symmetry of cubic and hexagonal phase leads to the change in the electronic energy levels and excited state dynamics of $Eu^{3+}$ doped ZnS. This is why hexagonal phase has stronger emission than cubic phase [17]. The Wurtzite structured ZnS nanophoshor host with enhanced properties modifies the optical characteristics by enhancing the intra-ion transition of $Eu^{3+}$ ions. The 4f-4f intra shell transitions in $Eu^{3+}$ enhance the photoluminescence properties of ZnS with broad emission bands [18].

This paper reports the hexagonal ZnS: $Eu^{3+}$ nanophosphor with varying concentrations 1, 2, 3, 10, 20 and 30% of $Eu^{3+}$ synthesized by solid state reaction method at low temperature. The increase in the grain size and crystallite size after doping of $Eu^{3+}$ ion, which increases the luminescence efficiency of the material is reported in this work. The photoluminescence peaks of the $Eu^{3+}$ doped ZnS nanoparticles have higher intensity compared to the data reported by Gurmeet Singh Lotey et al. [19]. Several authors have studied the photoluminescence characteristics of the undoped and $Eu^{3+}$ doped ZnS, but not reported the Judd-Ofelt (J-O) intensity parameters, Radiative emission transition probability ($A_T$), branching ratios and Energy transfer probability. Here we reported these parameters obtained from photoluminescence spectra, which is more accurate than that obtained from diffuse-reflectance and excitation spectra. The quenching of PL intensity in ZnS band and the enhancement of $Eu^{3+}$ doped ZnS after increasing $Eu^{3+}$ ion concentration reveals that $Eu^{3+}$ ions were present inside the ZnS host [20]. The $Eu^{3+}$ ions were on the surface of ZnS as reported by Mukherjee et al. The incorporation of $Eu^{3+}$ ions into ZnS lattice have more display applications due to its emission extended to longer wavelength [21]. The doping of $Eu^{3+}$ ion controls the PL emission and the radiative properties were explained with the help of Judd-Ofelt theory. The optical band gap energy and the refractive index of all the prepared samples were calculated and reported.

## 2. Experimental methods

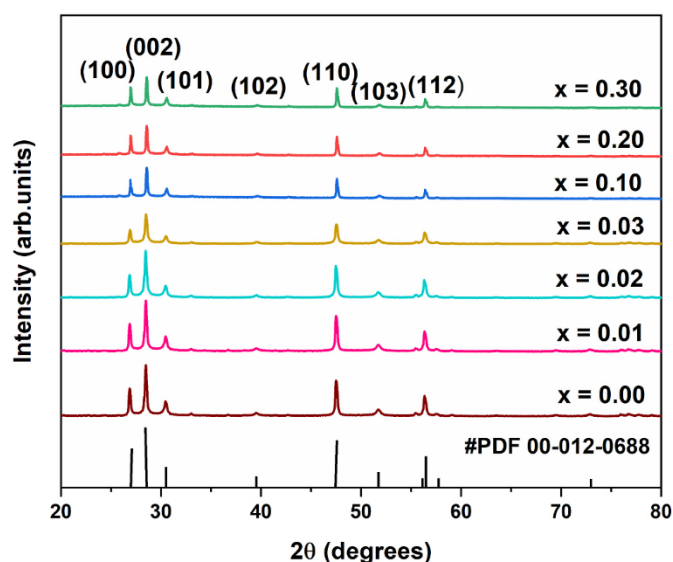Pure ZnS and varying concentration (1, 2, 3, 10, 20 and 30%) of $Eu^{3+}$



**Fig. 1.** XRD pattern of $Zn_{(1-x)}S:xEu^{3+}$ phosphors.

doped ZnS were prepared by solid state reaction method at low temperature. The zinc acetate Zn $(CH_3COO)_2 \cdot 2H_2O$ [Sigma-Aldrich, 99.9% purity] and sodium sulfide $Na_2S \cdot 9H_2O$ [Sigma-Aldrich, 99.9% purity] taken in 1:1 ratio is used as the starting materials for the synthesis of undoped ZnS nanomaterials. The suitable amounts of europium chloride, $EuCl_3 \cdot 6H_2O$ [Sigma-Aldrich, 99.9% purity] were taken to get the $Eu^{3+}$ doped ZnS nanoparticles. These chemicals were mixed and grinded using agate motor and pestle for about 16 h. The obtained powders were calcined at 400 °C for 5 h and grinded well to get fine powders of pure and $Eu^{3+}$ doped ZnS nanoparticles. The sample code for the synthesized materials were given as ZS2, EZS1, EZS2, EZS3, EZS4, EZS5 and EZS6 for pure ZnS, 1%, 2%, 3%, 10%, 20% and 30% Europium is added to ZnS lattice respectively.

The phase identification and the crystallinity were studied using Bruker D8 Advance diffractometer with Cu Kα radiation recorded with step size 0.02° per step time 0.5 s within the diffraction angle range 20–80°. The FTIR spectra or vibrational spectra were measured within the wavenumber range 400 $cm^{-1}$ to 4000 $cm^{-1}$ using IR Prestige-21 Spectrophotometer in a KBr matrix. The surface morphology was studied using Jeol 6390LA and elemental analysis by Oxford XMX N with an accelerating voltage 0.5–30 kV. The topography and morphology were studied using Joel JEM 2100 High Resolution Transmission Electron Microscopy (HRTEM) with an accelerating voltage 200 kV attached with SAED pattern. The composition of the materials was checked using energy dispersive X-ray spectroscopy (EDS) and induced coupled plasma mass spectroscopy (ICP-MS) using Thermoscientific model with Helium KED analysis mode. The reflectance spectra were recorded using Shimadzu UV–Vis Specrophotometer 2450 in the wavelength range 200–800 nm. The photoluminescence excitation (PLE) and emission (PL) spectra were done using Horiba Jobin-Yvon Fluoromax-4 and the decay measurements were recorded by PerkinElmer LS50 Spectrometer. The temperature dependent photoluminescence (TDPL) measurements were recorded using Hitachi 650–40 fluorescence spectrophotometer in 100 K–280 K temperature range.

## 3. Results and discussion

### 3.1. XRD analysis

The X-ray diffraction (XRD) patterns of all the samples were shown in Fig. 1. The diffraction peaks are sharp and highly intense indicating the high crystalline nature of the synthesized nanoparticles. All the diffraction peaks have been indexed in accordance with ICDD file no
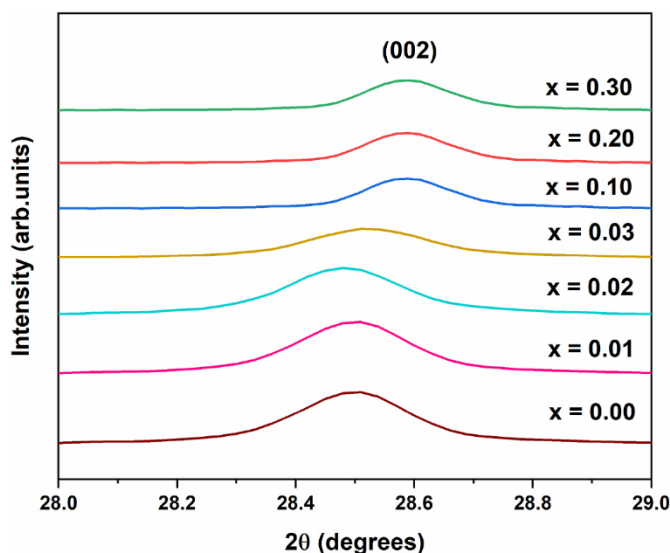
**Fig. 2.** XRD peak shift for maximum intensity peak (002).

#PDF 00-012-0688, corresponding to the hexagonal wurtzite structure of ZnS. The absence of diffraction peak corresponding to any other impurity material or secondary phase confirmed the purity of the synthesized material and the substitutional doping of Eu in the host ZnS. There is a shift of diffraction angles towards higher angle side when $Eu^{3+}$ is doped into ZnS lattice. This is due to the higher doping concentration, which increases the number of vacancies and causes the shifting of diffraction peaks towards higher angles [22]. The main reason for this shift is the large mismatch of the ionic radius between the $Zn^{2+}$ and $Eu^{3+}$ions. The ionic radius of $Eu^{3+}$ions is 0.95 Å, which is larger than that of $Zn^{2+}$ ions, which is 0.74 Å. Fig.2 shows the enlarged XRD spectra of maximum intensity peak (002).

The average crystallite size ($D_{hkl}$) of all the synthesized samples were calculated using the Debye Scherrer formula [23]:

$$D_{hkl} = \frac{0.9\,\lambda}{\beta cos\theta} \qquad (1)$$

where λ is the wavelength of the X-ray (Cu-kα radiation = 1.5406 Å source, β is the full width at half maximum in radian and θ is the Bragg angle. The average crystallite size calculated is in the range ≈37–44 nm. The parameters calculated from XRD are given in Table 1. From the XRD, the peaks intensity and the peak width were decreases with increase in $Eu^{3+}$ doping concentration. The variation of peak width with concentration is shown in Fig.3. As in figure, the peak width decreases as the concentration is increased, indicating a systematic increase in the crystalline size. The decrease of peak width may be due to the non-uniform lattice strain effect. According to Scherrer equation, peak width (β) is a function of crystallite size (D) and peak width contains the result of average dimension of the crystalline materials [24]. Also, the two simultaneous observations (width and intensity) are related with

the disordered lattice and the lattice strain induced in ZnS lattice due to the mismatch of ionic radius of $Zn^{2+}$ and $Eu^{3+}$ ions. This crystalline behavior increases the crystallite size and the quality of crystallinity [25]. The increase in crystallite size may be due to the difference in the ionic radius, that $Eu^{3+}$ doping may increase the agglomeration of crystallite size.

For hexagonal lattice structure, the lattice parameters $(a, b\,\&\,c)$ of the prepared phosphors were calculated from the following equations [26]:

$$\left[\frac{1}{d_{hkl}}\right]^2 = \left[\frac{h^2 + k^2 + l^2}{a^2}\right] + \frac{l^2}{c^2} \qquad (2)$$

where $d$ is the interplanar spacing and $h$, $k$ and $l$ representing the corresponding Miller indices of the plane. The unit cell volume ($V$) of the material can be calculated using the following relation [27]:

$$V = 0.866\,a^2 c \qquad (3)$$

The calculated lattice parameter and the cell volume are given in Table 1 and the slight differences in the values may be due to the mismatch of ionic radius of $Zn^{2+}$ (0.74 Å) and $Eu^{3+}$ (0.95 Å) ions. The Zn–S bond length (L) and the dislocation density (δ) were calculated using the equation [29]:

$$L = \left\{\frac{a^2}{3} + c^2\left[\frac{1}{2} - u\right]\right\}^{0.5} \qquad (4)$$

$$\delta = \frac{1}{D^2} \qquad (5)$$

where $u = \frac{a^2}{3c^2} + 0.25$ is the potential parameters representing the hexagonal structure, $(a\,\&\,c)$ are the calculated lattice parameters of the unit
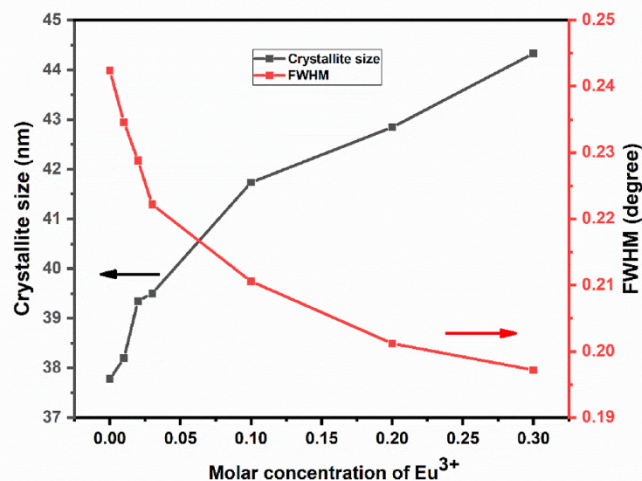


**Fig. 3.** Variation of Full width at half maximum (FWHM) and the crystallite size with respect to different molar concentrations of $Eu^{3+}$.

**Table 1**
Lattice parameters, cell volume, crystallite size, dislocation density, bond length of $Zn_{(1-x)}S{:}xEu^{3+}$ phosphors.

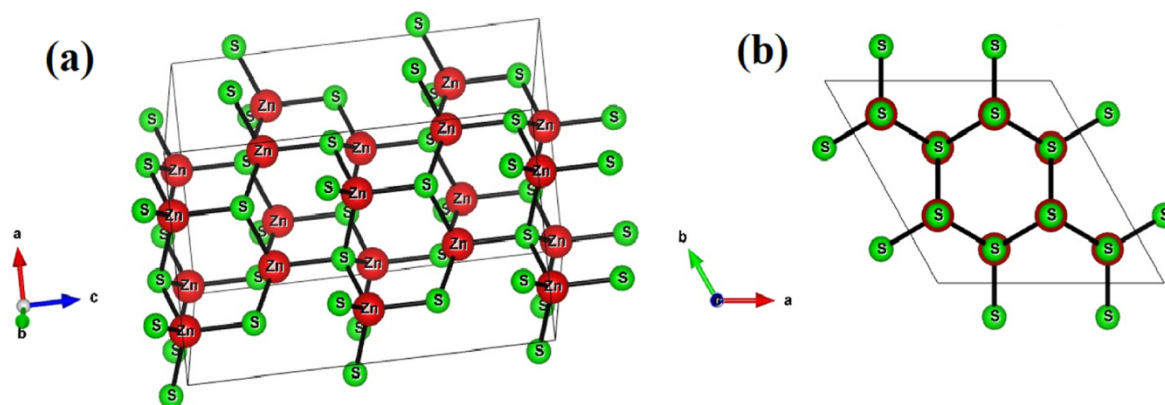| Sample Code | Lattice constants (Å) | | Unit cell volume (Å³) | Crystallite size (nm) | Dislocation Density, δ ($10^{15}$ line/m²) | Bond length, L (Å) |
|---|---|---|---|---|---|---|
| | a = b (Å) | c (Å) | | | | |
| ZS2 | 3.8137 | 6.2222 | 78.5300 | 37.7776 | 0.000701 | 2.339419 |
| EZS1 | 3.8153 | 6.2232 | 78.8371 | 38.1994 | 0.000685 | 2.339501 |
| EZS2 | 3.8183 | 6.2345 | 78.8571 | 39.3443 | 0.000646 | 2.346421 |
| EZS3 | 3.8186 | 6.2445 | 78.8757 | 39.5032 | 0.000641 | 2.342499 |
| EZS4 | 3.8231 | 6.2472 | 78.9927 | 41.7347 | 0.000574 | 2.340894 |
| EZS5 | 3.8249 | 6.2789 | 79.1522 | 42.8455 | 0.000545 | 2.33971 |
| EZS6 | 3.8288 | 6.2849 | 79.5519 | 44.3288 | 0.000509 | 2.33751 |

**Fig. 4.** (a) Full view of unit cell and (b) base view of unit cell of ZnS phosphor showing Hexagonal wurtzite structure drawn using VESTA software.

cell and $D$ is the average crystallite size of the material. The dislocation density and the Zn–S bond length were found to be increased by doping (Table 1) that can be attributed to the increase in crystallite size by doping, where defects increased after doping. The calculated bond length of the synthesized materials was close to that of bulk ZnS, L = 2.248 Å. The small difference in the bond length may be due to the doping which alters the ions in the ZnS [29]. The crystal structure of ZnS was generated and is shown in Fig. 4 (a) and the base view is shown in Fig. 4 (b). The both structures visualizations were obtained by the software called Visualization for Electronic and Structural Analysis (VESTA) using the structural parameters of ZnS [30]. The prepared ZnS phosphor is a hexagonal wurtzite structure with space group symmetry $P6_3mc$. The stacking sequence of close-packed planes is characterized by ABABAB repeating pattern. The structure can be defined as a number of alternative planes with tetrahedral coordinated $Zn^{2+}$ and $S^{2-}$ ions arranged on the c-axis [31].

As a refinement of Debye Scherrer approximation, the Williamson Hall (W–H) plots were plotted with $\beta cos\theta$ along y-axis and $4sin\theta$ along x-axis which gives a negative slope, which is physically meaningless. Therefore, the W–H method, an additive combination of both Lorentzian and Gaussian curves, is not applicable to these materials. The fits were close to the Gaussian curve than the Lorentzian curve [32].The size strain plots (SSP) of all the samples were shown in Fig. 5 and the parameters obtained from the graph are tabulated in Table 2. The SSP plots of the materials were obtained by plotting $(d_{hkl}\,\beta_{hkl}\,cos\theta_{hkl})^2$ on y axis and $(d_{hkl}^2\,\beta_{hkl}\,cos\theta_{hkl})$ on the x axis. The slope of the linear fit gives the average crystallite size and the intercept gives the RMS strain of the material. The line broadening resulting from the contribution of the microstrain gives a good result for the size-strain parameters of the materials [33]. The strain profile has a Gaussian function and the crystallite size profile describes a Lorentzian function given as [34],

$$(d_{hkl}\,\beta_{hkl}\,cos\theta_{hkl})^2 = \frac{1}{V_s}\left(d_{hkl}^2\,\beta_{hkl}\,cos\theta_{hkl}\right) + \left(\frac{\varepsilon_a}{2}\right)^2 \quad (6)$$

where $d_{hkl}$ is the inter planar spacing in (h k l) planes, $V_s$ is the volume of average weighted crystallite size and $\varepsilon_a$ is the amount of shear strain associated with the root mean square (RMS) value of strain, $\varepsilon_{rms}$.

$$\varepsilon_{rms} = \frac{\varepsilon_a}{2\sqrt{2\pi}} \quad (7)$$

The best method suited for the material is the size strain plot method which gives positive slopes and positive y-intercepts. According to literature reports, SSP method is the best method compared with the W–H methods, because the data from the high angle reflections are less sensitive and the data points are closer to the linear fit. The lattice strain present in the materials may be arising due to dislocations and deformations. This will lead to XRD peak broadening in the materials and

the strain is considered to be the degree of the lattice distortion [35].

### 3.2. FTIR spectra

The FTIR spectra of pure and Eu doped ZnS nanoparticles were shown in Fig. 6. All the FTIR measurements were carried out by mixing the samples with KBr, some water molecules were absorbed since KBr is hygroscopic. The FTIR bands were observed in 3512.86 cm$^{-1}$, 1596.06 cm$^{-1}$, 1517.96 cm$^{-1}$, 1446.48 cm$^{-1}$, 1204.24 cm$^{-1}$, 1126.13 cm$^{-1}$, 1082.45 cm$^{-1}$, 976.55 cm$^{-1}$, 849.47 cm$^{-1}$ 574.13 cm$^{-1}$ for undoped ZnS nanoparticles. The broad peak appears at 3512.86 cm$^{-1}$, 3563.16 cm$^{-1}$, 3584.34 cm$^{-1}$, 3573.75 cm$^{-1}$, 3555.22 cm$^{-1}$, 3655.82 cm$^{-1}$ and 3670.38 cm$^{-1}$ of all the samples are due to the O–H stretching vibrations of water [36]. The peaks at 574.13 cm$^{-1}$, 648.26 cm$^{-1}$, 662.62 cm$^{-1}$, 669.44 cm$^{-1}$, 648.26 cm$^{-1}$, 633.69 cm$^{-1}$, 612.52 cm$^{-1}$ of all the samples are ZnS bands that correspond to sulfide [37]. The band at 1082.45 cm$^{-1}$, 983.17 cm$^{-1}$, 961.98 cm$^{-1}$, 940.81 cm$^{-1}$, 1139.37 cm$^{-1}$, 1075.83 cm$^{-1}$, 1069.21 cm$^{-1}$ could be associated with S–O–S stretching vibrations. There is some weak additional bonds in all the samples indicate the presence of resonance interaction between vibrational modes of sulphide ions in the crystal. The peak assignments of all the samples are shown in Table 3. The results were good agreement with the reported literature [13].

### 3.3. HRTEM

HRTEM is a powerful and unique way to identify the electronic structures of nanocrystals using an electron probe in the nanometer range [38]. Fig. 7a and b shows the TEM images of 0.1Eu$^{3+}$: ZnS. The average particle size calculated is 68.8 nm. The particles are almost elliptical in shape with very good uniformity. Fig. 7c shows the lattice fringes images and the d spacing calculated is 2.4 Å matches very well with (102) plane of ZnS nanoparticles. The selected area diffraction (SAED) pattern having bright spots, shown in Fig. 7d confirms the crystalline nature of the prepared materials. Fig. 7e represents the particle size histograms calculated using IMAGE J software. The most visible particle sizes obtained for 0.1Eu$^{3+}$: Zn$_{0.9}$S samples are 73 nm, 67 nm 64 nm, 69 nm, 75 nm, 71 nm, 65 nm, 68 nm, 69 nm and 67 nm respectively. The particles are showed an inhomogeneous distribution with small particles of sizes 64 nm–75 nm are agglomerating into larger clusters.

### 3.4. SEM analysis

Fig. 8 shows typical scanning electron microscopy (SEM) images of Zn$_{(1-x)}$S:xEu$^{3+}$ (a) x = 0.01 and (b) x = 0.1 phosphor materials. The samples have similar morphologies. The grains present in the materials have irregular shape and micrometer size. This microstructure confirms
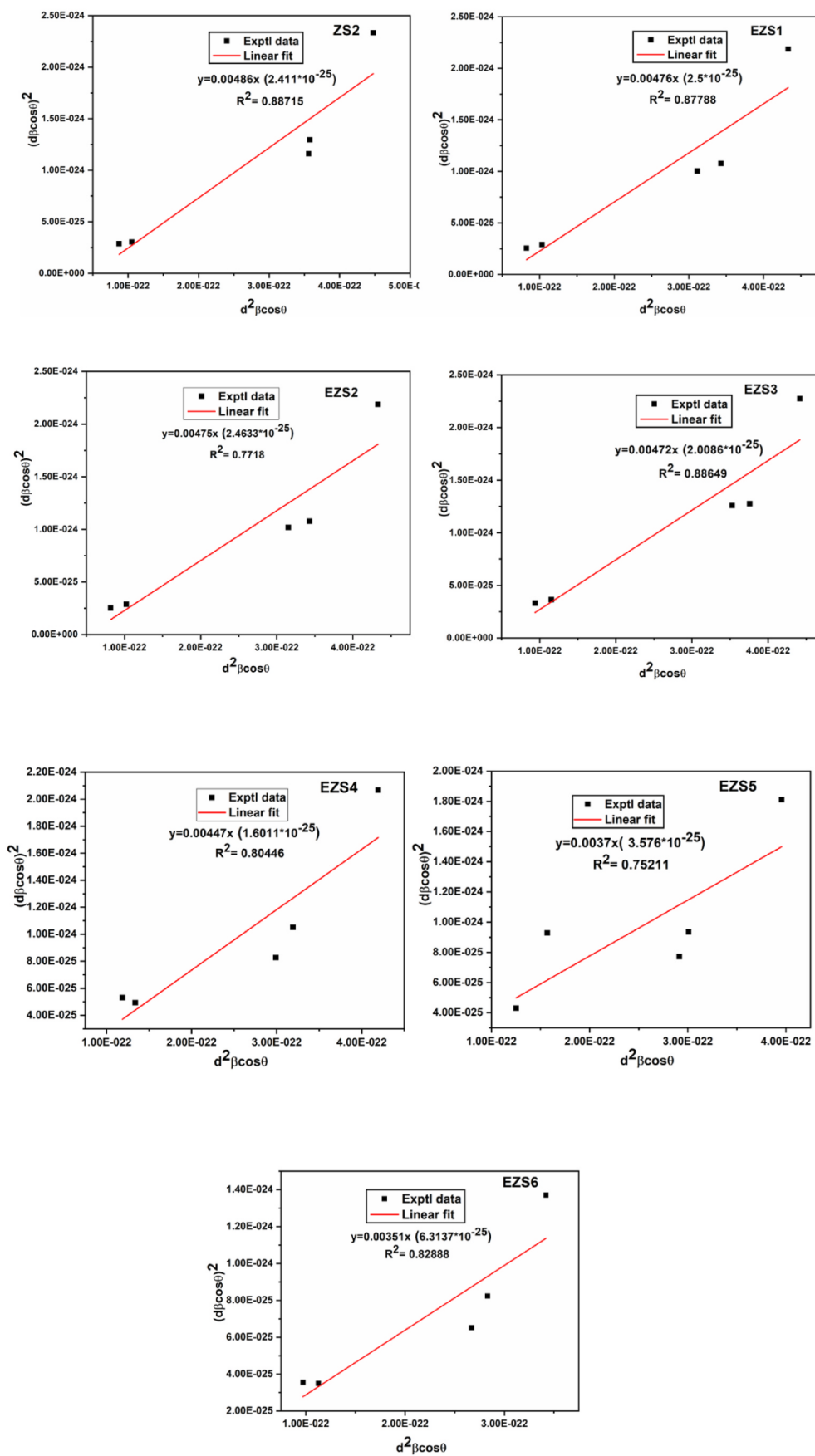
**Fig. 5.** Size-Strain Plot of $Zn_{(1-x)}S:xEu^{3+}$ phosphor materials.

**Table 2**
Lattice strain and crystallite size from SSP plot of $Zn_{(1-x)}S{:}xEu^{3+}$ phosphor materials.

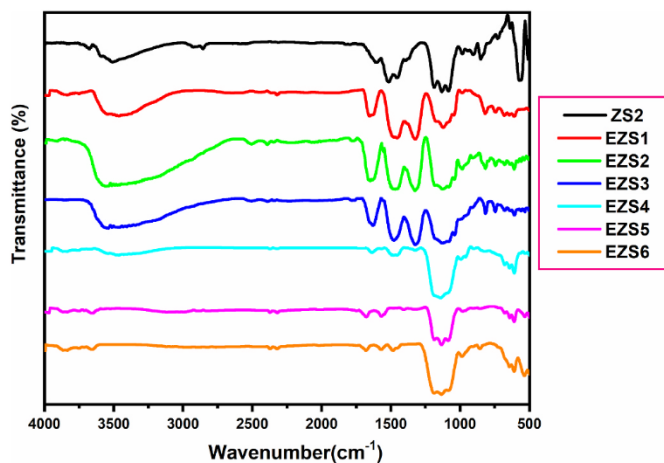| Sample Code | $D_v$ (nm) | Strain $\varepsilon$ | | Correlation Coefficient R |
|---|---|---|---|---|
| | | $\varepsilon_a$ | $\varepsilon_{rms}$ | |
| ZS2 | 27.4348 | 3.1055 | 0.6099 | 0.8495 |
| EZS1 | 28.0112 | 3.1625 | 0.6212 | 0.8377 |
| EZS2 | 28.0702 | 3.1389 | 0.6166 | 0.8368 |
| EZS3 | 28.3688 | 2.8341 | 0.5567 | 0.8410 |
| EZS4 | 29.8285 | 3.7894 | 0.7443 | 0.8969 |
| EZS5 | 36.0361 | 3.7417 | 0.7349 | 0.8075 |
| EZS6 | 37.9867 | 2.9786 | 0.5851 | 0.7718 |



**Fig. 6.** FTIR spectra of $Zn_{(1-x)}S{:}xEu^{3+}$ phosphor materials.

the crystallinity of the prepared materials [39]. The grain size is estimated and given in Table 4. The grain size increases with $Eu^{3+}$ ion concentration. This is like the crystallite size obtained from the XRD results. The grain size increases when the dislocation density decreases due to doping of $Eu^{3+}$. The SEM images show that the powdered phosphor particles were uniformly distributed throughout the surface [40].

### 3.5. EDS analysis

The EDS spectra of $Zn_{(1-x)}S{:}xEu^{3+}$ ($x = 0.01$ and $x = 0.1$) phosphor materials are shown in Fig. 9a and b respectively. The EDS indicate that the prepared materials have an elemental composition of Zn, S and Eu. The atomic and weight percentages of the synthesized samples were shown in Table 5. The amount of elements present was close to the expected values. The EDS analysis confirmed the doping of $Eu^{3+}$ ions in ZnS lattice in the $Zn_{(1-x)}S{:}xEu^{3+}$ phosphor materials. The doping concentration of $Zn_{(1-x)}S{:}xEu^{3+}$ ($x = 0.3$) phosphor materials obtained from ICP-MS indicating the doping amount is 28.31% mmol.

### 3.6. UV–vis spectroscopy

The UV–Vis absorption spectra of the pure ZnS and $Eu^{3+}$ doped ZnS samples are shown in Fig. 10a and b. The absorption edge is found to be red shifted from 419 nm to 388 nm after $Eu^{3+}$ doping. The absorption edge shift towards higher wavelength side with increasing crystallite size is clearly manifest from the absorption spectra. The absorption edge at 419 nm for pure ZnS is due to the inter-band or band-edge absorption happens to excite electrons from valance band to conduction band. For $Eu^{3+}$ doped ZnS, the maximum absorption peak is at 388 nm, which corresponds to transition $4f^7 \rightarrow 4f^6 5 d^1$ of Europium ions. It is clear from the picture that all the $Eu^{3+}$ doped ZnS materials have a generation of two additional absorption bands. The two impurity bands are in the near infra-red (NIR) region and this band is absent in the undoped ZnS material. This additional NIR band is created due to the formation of a doping band (DB) within the energy band gap of the ZnS, which is located close to the valence band. Therefore, the optical absorption takes place in both undoped ZnS and $Eu^{3+}$ doped ZnS are quite different. The different path of optical absorption is shown in Fig. 10d. In the case of undoped ZnS, the photons are absorbed through the 'A' path of the direct transition of the electrons from the valence band to the conduction band. On the other hand, for $Eu^{3+}$ doped ZnS, since at room temperature, the donor band is fully populated, the absorption occurs in two stages:1) from valence band to donor band via path 'B' and 2) from donor band to conduction band via path 'C'. These transitions are responsible for the generation of NIR absorption peak at around 730 nm in $Eu^{3+}$ doped ZnS phosphor materials [41]. The optical band gap energy ($E_g$) of the prepared samples can be obtained from the Wood and Tauc's equation [40]:

$$\alpha h\nu = A\left(h\nu - E_g\right)^n \qquad (8)$$

where $\alpha$ is the optical absorption coefficient, $h\nu$ is the photon energy, $A$ is a constant and $n$ which determines the transition causing this absorption. The value for $n$ is $n = 2$ for direct band gap and $n = \frac{1}{2}$ for indirect transition. ZnS is a direct band gap semiconductor reported by several authors [42]. The band gap of the samples assuming direct transition was plotted between $(\alpha h\nu)^2$ as a function of $h\nu$. The band gap energy found to be decreasing and this is due to the defects or the introduction of new energy level in the ZnS band structure. Fig. 10c represents the Tauc plot of all the samples. The optical band gap energy and the absorbance edge of all the prepared samples were tabulated in Table 6.

The band gap energy was found to be decreasing from 3.59 eV to 3.43 eV after doping with $Eu^{3+}$ ions. This band gap shrinkage is due to the heavy doping density. This response can be explained by the fact that as the concentration of impurities increases, the wave functions of electrons attached to the impurity atoms begin to overlap. This overlap strengthens the energy to a different level than the energy band. This impurity band reduces the band gap energy of the material. The optical band gap energy of $Eu^{3+}$ doped ZnS calculated using Tauc plot is ranging from $\approx$3.13 to 5.5 eV according to literature survey studies [43]. This variation due to size effects is peculiar and therefore the high values of
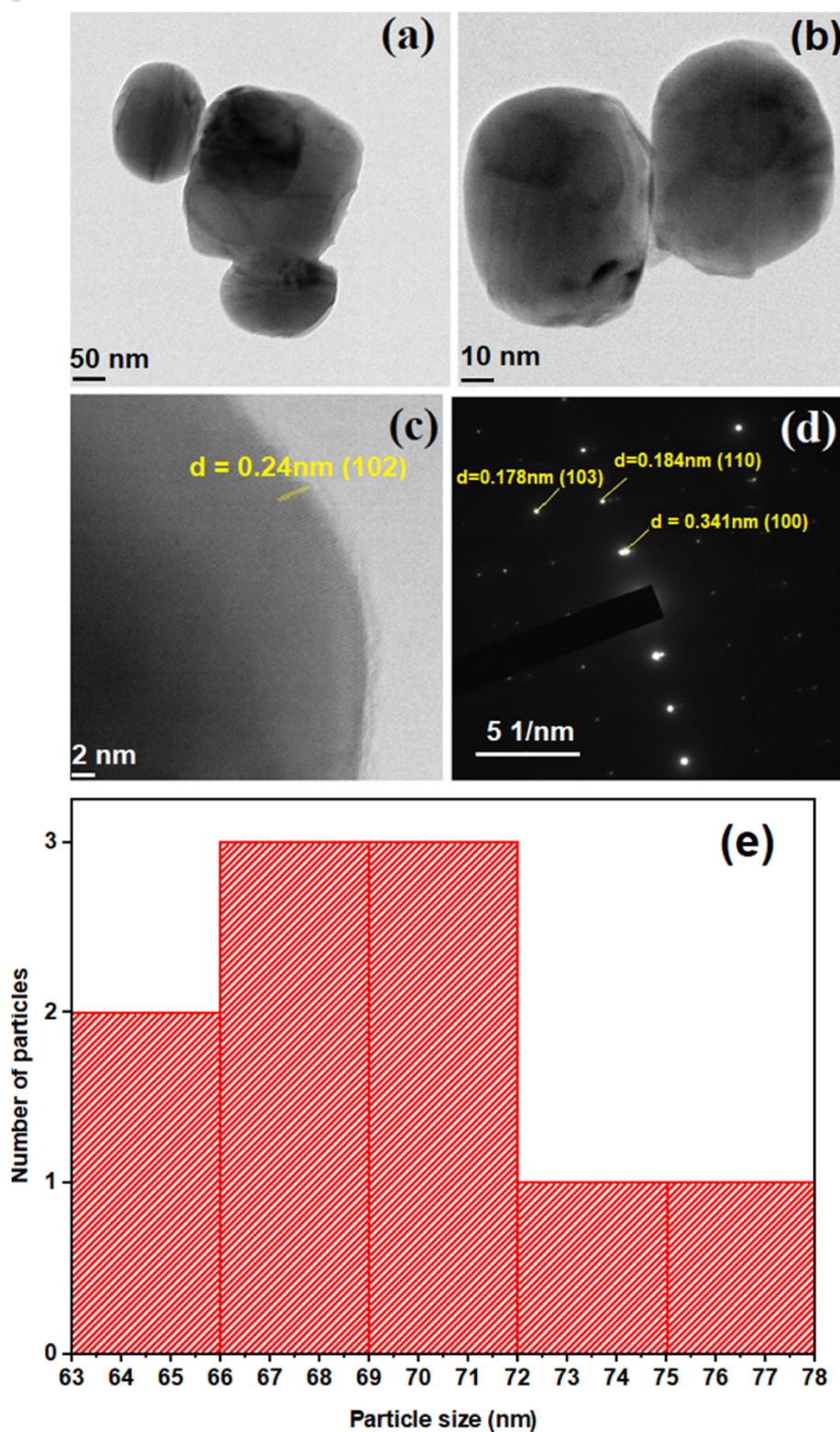
**Table 3**
Peak assignments of FTIR spectra of all the samples.

| ZS2 | EZS1 | EZS2 | EZS3 | EZS4 | EZS5 | EZS6 | Peak Assignments |
|---|---|---|---|---|---|---|---|
| 3512.86 | 3563.16 | 3584.34 | 3573.75 | 3555.22 | 3655.82 | 3670.38 | O–H Stretching vibrations |
| 1596.06 | 2308.25 | 2379.67 | 2501.51 | – | 2373.11 | 2365.16 | $CO_2$ Stretching vibrations |
| 1517.96 | 1652.98 | 1646.36 | 1625.19 | 1646.37 | 1674.17 | 1682.11 | C–O–S Vibrations |
| 1446.48 | 1472.97 | 1461.04 | 1482.22 | 1498.11 | 1560.33 | 1566.94 | Symmetric starching vibrations |
| 1204.24 | 1311.46 | 1318.07 | 1324.69 | 1328.67 | 1189.67 | 1189.53 | O–H Bending vibrations |
| 1126.13 | 1111.57 | 1118.19 | 1126.13 | 1204.24 | 1132.75 | 1133.12 | C–O stretching vibrations |
| 1082.45 | 983.17 | 961.98 | 940.81 | 1139.37 | 1075.83 | 1069.21 | S–O–S stretching vibrations. |
| 976.55 | 812.41 | 883.88 | 819.02 | 961.98 | 983.17 | 984.12 | Formation of tetrahedral coordinated Zn |
| 849.47 | 734.36 | 747.54 | 740.92 | 684.00 | 677.38 | 854.76 | Asymmetric bending |
| 574.13 | 648.26 | 662.62 | 669.44 | 648.26 | 633.69 | 612.52 | ZnS stretching vibrations |

**Fig. 7.** (a) & (b) TEM images, (c) HRTEM images, (d) SAED patterns and (e) particle size histograms of the $Zn_{0.9}S{:}0.1Eu^{3+}$ phosphor material.

optical band gap estimated from Tauc plot are not stable. The reason is, in ZnS, the lowest valance band is constructed by 3s band electrons of S, the middle valance bands have 3d band electrons of Zn and the upper valance bands have 3p band electrons of S states while the conduction bands are composed from the 4s band electrons of Zn [6]. The absorption spectra of ZnS involve the optical transition in the UV–Vis region and the outbreak of lowest energy transfer is given by the optical band gap. Due to this reason, the Tauc plot must be done in the lower energy region to decrease the probability of getting higher values of optical band gap energy. Here, the band gap energy of the prepared materials, ranges from 3.59 to 3.43 eV, are in good agreement with the previous reported papers. Mateus M Ferrer et al., had reported band gap energy in
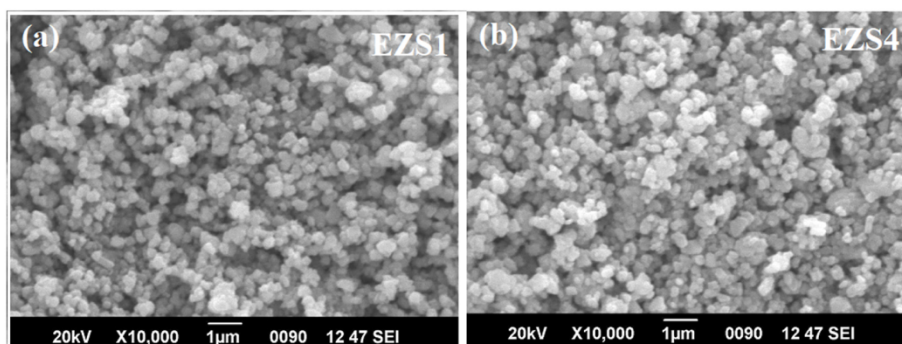
**Fig. 8.** SEM images of $Zn_{(1-x)}S{:}xEu^{3+}$ (a) x = 0.01 and (b) x = 0.1 phosphor materials.

**Table 4**
Calculated average grain size of $Zn_{(1-x)}S{:}xEu^{3+}$ (x = 0.01 and x = 0.1) phosphor materials.

| Sample Code | Grain size (nm) |
|---|---|
| EZS1 | 193.09 |
| EZS4 | 213.34 |

the range ≈3.72–3.55 eV for undoped and $Eu^{3+}$ doped ZnS by microwave-assisted solvothermal (MAS) method [16]. Mou Pal et al., reported undoped and $Eu^{3+}$ doped ZnS nanoparticles by a wet chemical route varying band gap ≈3.82–3.79eV range [44]. Zhiren Wei et al., reported the undoped and $Eu^{3+}$ doped ZnS with band gap ranging from ≈3.295 to 3.141 eV synthesized by hydrothermal method [45].

### 3.7. Photoluminescence, Judd-Ofelt and radiative studies

The excitation spectra of $Zn_{0.9}S{:}0.1Eu^{3+}$ phosphor shown in Fig.11 consists of charge transfer (CT) band and a series of sharp bands in the 250–500 nm range. These sharp bands are originated due to the intra configurational $4f-4f$ transitions of $Eu^{3+}$ rare earth ions [46]. The CT bands are formed from the $S^{2-}$ anion's filled 2p orbitals to the 4f orbitals of the $Eu^{3+}$ ions. The excitation spectra have an intense peak located at 390 nm corresponding to $^7F_0-^5L_6$ transitions. The two other strong peaks at 415 nm and 464 nm are corresponds to $^7F_0-^5D_3$ and $^7F_0-^5D_2$ transitions [47]. The photoluminescence emission spectra of pure ZnS and $Eu^{3+}$doped samples were measured at room temperature using a xenon lamp as the light source and the results were shown in Fig. 12a and b. The PL studies are hardly associated with surface states, oxygen vacancies, defects and stoichiometry of the semiconductor material.

The emission spectra of pure ZnS nanophosphor at excitation wavelength 286 nm give intense broad and strong emission centered at 551 nm. The peak shows the surface defects and vacancies which acts as energy traps and nonradiative centers in pure ZnS. This will quench the photoluminescence of pure ZnS phosphor material [48]. The emission at

403 nm may be attributed to near band edge emissions, the characteristics of a semiconductor material [49]. The PL spectra of $Eu^{3+}$ doped samples show a broad band in the range 450–510 nm with maximum intensity at ~465 nm. This may due to ZnS host matrix and the emission profile is based on multi-phonon and multilevel interactions. That means if a system attaining relaxation through several paths involving multiple states within the band gap energy of the ZnS semiconductor material [50]. Also the spectra shows five sharp peaks between 550 nm and 710 nm, indicating that the surface defects were removed after doping europium. The five emission bands centered at about 578 nm, 590 nm, 614 nm, 650 nm and 700 nm were corresponding to $^5D_0$-$^7F_0$, $^5D_0$-$^7F_1$, $^5D_0$-$^7F_2$, $^5D_0$-$^7F_3$ and $^5D_0$-$^7F_4$ intra-4f transitions of $Eu^{3+}$ ions respectively [51]. These observed emission bands give the site symmetry of $Eu^{3+}$ ions in the ZnS material. The bands at 578 nm, yellow emission, are attributed to the sulfur vacancies at the interface of ZnS grains and are assigned to trivalent europium transition [52]. The orange emission at 590 nm was assigned to the sulfur element present on the surface of ZnS nanoparticle. The red emission at 614 nm is due to the efficient transfer of energy from ZnS to $Eu^{3+}$ ions. The emission at 650 nm present in three concentrations of ZnS:$Eu^{3+}$ nanomaterials (3,10 and 20%) have intensity due to J-mixing [53]. The concentrations 1, 2 and 30% missed this transition due to the weak J-mixing. The emission at 700 nm was

**Table 5**
The atomic percentages of elements of $Zn_{(1-x)}S{:}xEu^{3+}$ (x = 0.01 and 0.1) phosphor material calculated from EDS spectra.

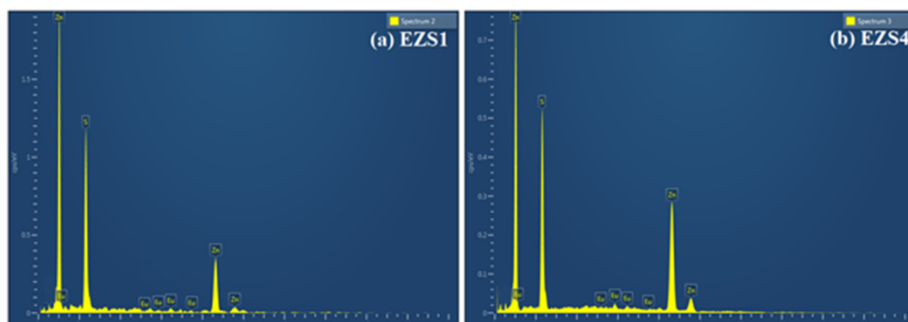|  | Element | Calculated atomic percentage (%) | Measured atomic percentage (%) |
|---|---|---|---|
| $Zn_{0.99}Eu_{0.01}S$ | S | 50 | 49.77 |
|  | Zn | 49.5 | 49.69 |
|  | Eu | 0.5 | 0.54 |
|  |  | 100 | 100 |
| $Zn_{0.9}Eu_{0.1}S$ | S | 50 | 50.44 |
|  | Zn | 45 | 45.39 |
|  | Eu | 5 | 4.17 |
|  |  | 100 | 100 |



**Fig. 9.** EDS spectrum of $Zn_{(1-x)}S{:}xEu^{3+}$ (a) x = 0.01 and (b) x = 0.1 phosphor materials.
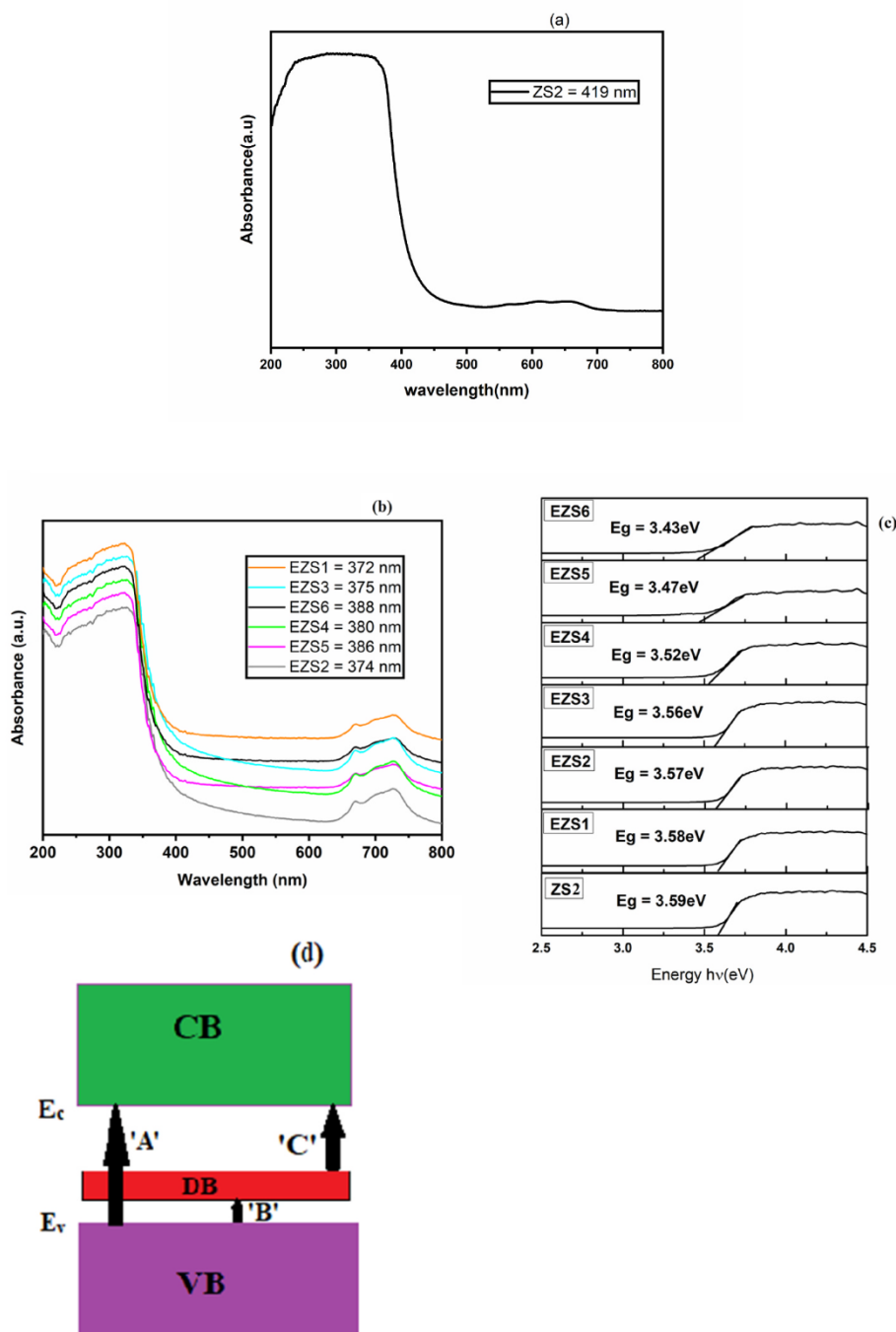
**Fig. 10(a).** Absorbance spectra of undoped ZnS, (b) Absorbance spectra of $Eu^{3+}$ doped ZnS, (c) Tauc plot of all the samples and (d) Schematic representation of band diagram of $Eu^{3+}$ doped ZnS and related optical transitions.

**Table 6**
Absorption edge and band gap values of all the samples.

| Sample code | Absorption edge (nm) | Band gap(eV) |
|---|---|---|
| Bulk ZnS | 345 | 3.59 |
| ZS2 | 419 | 3.59 |
| EZS1 | 372 | 3.58 |
| EZS2 | 374 | 3.57 |
| EZS3 | 375 | 3.56 |
| EZS4 | 380 | 3.52 |
| EZS5 | 386 | 3.47 |
| EZS6 | 388 | 3.43 |

explained using the ZnS electronegativity was recently reported by Ahemen et al. These five impurity bands of $Eu^{3+}$ ions in ZnS are in good agreement with the literature. Yongbo Wang et al., reported the incorporation of $Eu^{3+}$ ions in ZnS semiconductor and studied their photoluminescence spectroscopy using chemical method. The band edge emission was obtained at 418 nm and the sharp bands at 590, 618 and 695 nm were assigned $^5D_0$-$^7F_1$, $^5D_0$-$^7F_2$ and $^5D_0$-$^7F_4$ transitions respectively. These cubic structured materials are having applications in biomedical field [54]. Gurmeet Singh Lotey et al., reported pure and Eu-doped ZnS nanoparticles have been prepared by chemical precipitation method. The prepared material was in cubic structure with average size 29–37 nm. The band gap calculated for pure ZnS as 4.2 eV
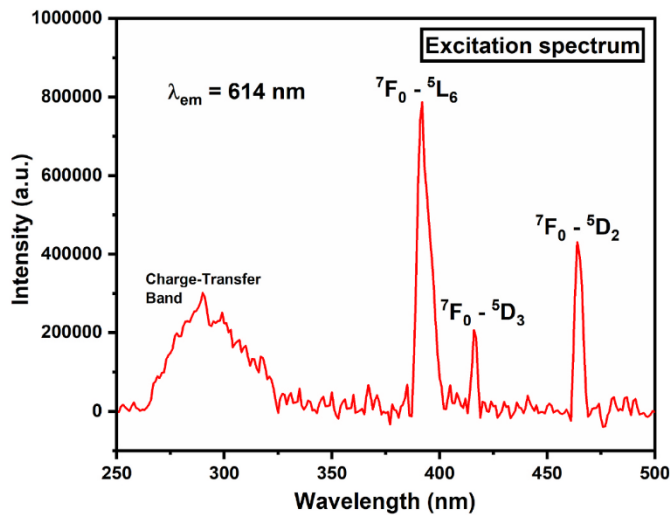
**Fig. 11.** Excitation spectra of ZnS:0.1Eu$^{3+}$ phosphor material.



and decreases up to 3.9 eV after doping Eu$^{3+}$. The PL spectra shows five emission peaks at 574, 591, 617, 700, 754 nm for Eu doped ZnS nanoparticles corresponding to $^5D_0$-$^7F_0$, $^5D_0$-$^7F_1$, $^5D_0$-$^7F_2$, $^5D_0$-$^7F_3$ and $^5D_0$-$^7F_4$ transitions [55]. Sabit Horoz et al., studied the photoluminescence properties of Eu doped ZnS by wet chemical method to form cubic structure. They reported three sharp emission bands at 591 nm, 616 nm and 700 nm which are corresponding to $^5D_0$-$^7F_1$, $^5D_0$-$^7F_2$ and $^5D_0$-$^7F_4$ transitions [56]. Lun Ma et al., reported most intense violet emission at 420 nm and four sharp emissions at 596 nm, 617 nm, 652 nm and 699 nm corresponds to transitions $^5D_0$-$^7F_1$, $^5D_0$-$^7F_2$, $^5D_0$-$^7F_3$ and $^5D_0$-$^7F_4$ levels when Eu$^{3+}$ is doped into ZnS lattice. The materials were prepared by solid state reaction method at 800 °C at 3 h s [57]. The $^5D_0$-$^7F_1$ transition at 590 nm (orange emission) is assigned to be magnetic dipole (MD) and $^5D_0$-$^7F_2$ transition at 614 nm (red emission) corresponds to hypersensitive electric dipole (ED) transition with selection rule $\Delta J = 2$ [56]. The majority transitions in the spectrum are assigned to be induced ED transitions or forced ED transitions which are weaker than ordinary ED transitions and allow transitions with odd parity. The MD transitions are weak or comparable with the induced ED transitions and it is independent of surroundings and it allows transition with even parity. The intensity of MD transition is weak compared with the forced ED transitions. The MD transition is mostly independent of environment and ED transition depends largely on environment [59]. Therefore, the site symmetry of Eu$^{3+}$ ions was in a site with inversion symmetry. The $^5D_0$-$^7F_0$ (578 nm) transition is very weak compared with $^5D_0$-$^7F_1$ transition. According to Judd-Ofelt (J-O) theory, the $^5D_0$-$^7F_{0,3,5}$ transitions are strictly forbidden. The $^5D_0$-$^7F_0$ transition has maximum intensity for EZS1 material, minimum intensity for EZS3 material and the peak is absent only for EZS6 material. The presences of this transition violate the selection rule of J-O theory [60]. This transition may be due to the incorporation of low energy charge transfer states into the quantum states of the 4f$^6$ configuration. This low energy induces the crystal field splitting which again enhances the $^5D_0$-$^7F_0$ transition. The $^5D_0$-$^7F_1$ transition has maximum intensity for EZS4 material and minimum intensity for EZS6 material. The $^5D_0$-$^7F_2$ transition intensity is the most intense, but $^5D_0$-$^7F_1$ transition also has a remarkable intensity. The $^5D_0$-$^7F_2$ transitions were responsible for the red-light emission occurred in the phosphor materials and the maximum intensity was obtained for EZS4 material. These transitions were directly proportional to the J-O parameter $\Omega_2$. The red emission found at 614 nm arises from the radiative recombination among the interstitial zinc states and zinc vacancies [61]. For the EZS1, EZS2 and EZS6 samples, the $^5D_0$-$^7F_3$ transition is absent in the spectra due to weak incorporation of low energy charge transfer states into the quantum states of the 4f$^6$ configuration and the
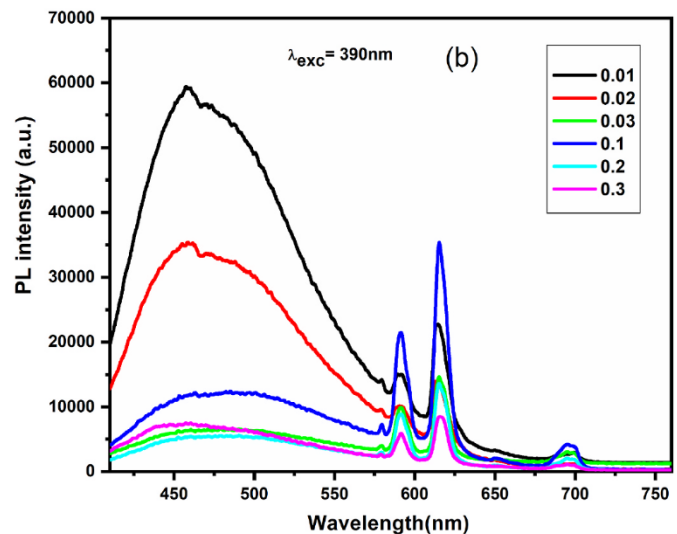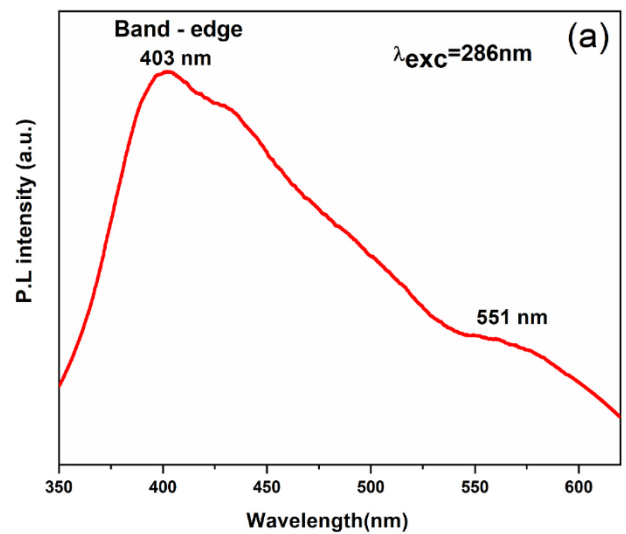
**Fig. 12.** Emission spectrum of (a) pure ZnS under excitation of 286 nm and (b) Zn$_{(1-x)}$S:$x$Eu$^{3+}$. ($x = 0.01$, 0.02, 0.03, 0.1, 0.2 & 0.3) phosphor under excitation of 390 nm.

intensity was maximum for EZS4 material. The $^5D_0$-$^7F_4$ transition intensity is weaker than $^5D_0$-$^7F_2$ transition. For EZS3 samples; the luminescence intensity of $^5D_0$-$^7F_1$ MD transition is same as that of $^5D_0$-$^7F_2$ ED transition. Moreover, the electric quadrupole transitions also occur in the compounds with even parity transition, but having less intensity than MD transitions and induced ED transitions. But there is no convincing evidence for the occurrence of electric quadrupole transitions in Eu$^{3+}$ ions. The luminescence intensity is strong for Eu$^{3+}$ doped EZS1 and EZS2 samples since Eu$^{3+}$ occupies the sites without an inversion center. On increasing the concentration of europium, the intensity decreases may be explained using the phenomenon of concentration quenching [62]. The emission intensity depends on crystallite size, grain size, doping effects, dependence between host and activator, defects and luminescence centers. From this observation, we can conclude that Eu$^{3+}$ ions were filled sites with distinct symmetry for different doping concentrations. The decrease in emission intensity with increasing Eu$^{3+}$ concentration may be due to the increase of non-radiative recombination centers in the luminescence mechanism [63]. There is a charge difference between Zn$^{2+}$ and Eu$^{3+}$ ions, so Eu$^{3+}$

**Table 7**

Chromaticity co-ordinates (*x, y*), color purity and correlated color temperature (CCT) and energy transfer efficiency ($\eta_{ET}$) of $Zn_{(1-x)}S:xEu^{3+}$ (x = 0.01, 0.02, 0.03, 0.1, 0.2 & 0.3) phosphor.

| Sample Code | CIE coordinates | | Color Purity (%) | CCT(K) | $\eta_{ET}$ (%) | Refrative index, n |
|---|---|---|---|---|---|---|
| | x | Y | | | | |
| EZS1 | 0.6091 | 0.3910 | 97.07 | 1628.58 | 8.12 | 2.254 |
| EZS2 | 0.5542 | 0.4451 | 79.37 | 1979.24 | 14.53 | 2.262 |
| EZS3 | 0.6261 | 0.3732 | 98.84 | 1758.39 | 2.96 | 2.260 |
| EZS4 | 0.6090 | 0.3905 | 90.41 | 1629.26 | 22.83 | 2.261 |
| EZS5 | 0.6081 | 0.3914 | 97.72 | 1626.87 | 2.95 | 2.265 |
| EZS6 | 0.5995 | 0.3999 | 97.21 | 1622.10 | 3.09 | 2.299 |

**Table 8**

Radiative properties for the prominent emission transitions of $Zn_{(1-x)}S:xEu^{3+}$ (x = 0.01, 0.02, 0.03, 0.1, 0.2 & 0.3) phosphor material.

| Parameter | EZS1 | EZS2 | EZS3 | EZS4 | EZS5 | EZS6 |
|---|---|---|---|---|---|---|
| $\Omega_2$ ($\times 10^{-22}$ cm$^2$) | 0.7049 | 0.5975 | 1.7875 | 2.0412 | 1.6915 | 0.5448 |
| $\Omega_4$ ($\times 10^{-22}$ cm$^2$) | 0.1692 | 0.1036 | 0.6263 | 0.4207 | 0.6299 | 0.1188 |
| $R_{02}$ | 0.5933 | 0.6973 | 0.2224 | 0.2025 | 0.2426 | – |
| $R_{21}$ | 1.5320 | 1.3499 | 1.5281 | 1.6352 | 1.5152 | 1.4417 |
| $R_{41}$ | 0.1538 | 0.0793 | 0.2239 | 0.1995 | 0.2361 | 0.1862 |
| Radiative parameter | EZS1 | EZS2 | EZS3 | EZS4 | EZS5 | EZS6 |
| $A_R$ (s$^{-1}$) | 216.98 | 197.21 | 446.72 | 523.26 | 466.27 | 135.77 |
| $A_{NR}$ (s$^{-1}$) | 424.79 | 469.27 | 335.49 | 258.07 | 328.87 | 726.81 |
| $A_T$ (s$^{-1}$) | 641.76 | 666.48 | 782.21 | 781.33 | 795.14 | 862.58 |
| $\tau_{rad}$ (ms) | 4.61 | 5.07 | 2.2385 | 1.9111 | 2.144 | 7.365 |
| $\tau_{obs}$ (ms) | 1.5588 | 1.4971 | 1.2783 | 1.2699 | 1.2572 | 1.1599 |
| $\eta_{int}$ (%) | 33.81 | 29.59 | 57.11 | 66.97 | 58.64 | 15.74 |
| $\eta_{ex}$ (%) | 17.34 | 14.53 | 25.72 | 34.31 | 33.34 | 13.82 |
| $W_{NR}$(ms) | 0.4246 | 0.4707 | 0.3356 | 0.2642 | 0.3290 | 0.7264 |
| $\beta_{01}$(%) | 25.97 | 27.59 | 33.72 | 29.55 | 29.88 | 36.83 |
| $\beta_{02}$(%) | 41.26 | 38.63 | 53.44 | 50.12 | 46.96 | 55.07 |
| $\beta_{04}$(%) | 4.72 | 3.19 | 8.93 | 6.97 | 8.34 | 8.11 |
| $\sigma_{01}$ ($\times 10^{-20}$ cm$^2$) | 1.0027 | 2.6299 | 5.1808 | 5.255 | 4.7732 | 1.9941 |
| $\sigma_{02}$ ($\times 10^{-20}$ cm$^2$) | 3.1167 | 8.8385 | 9.1862 | 10.365 | 8.3945 | 2.6961 |
| $\sigma_{03}$ ($\times 10^{-20}$ cm$^2$) | 0.3852 | 5.2563 | 1.6349 | 1.4606 | 1.5865 | 4.9213 |
| $\sigma_{01} \times \Delta\lambda_{eff}$ ($\times 10^{-28}$ cm$^3$) | 1.8075 | 2.8221 | 4.8037 | 4.9314 | 4.4256 | 1.5412 |
| $\sigma_{02} \times \Delta\lambda_{eff}$ ($\times 10^{-28}$ cm$^3$) | 3.3233 | 1.7419 | 8.8095 | 9.6775 | 8.0481 | 2.6661 |
| $\sigma_{03} \times \Delta\lambda_{eff}$ ($\times 10^{-28}$ cm$^3$) | 0.6426 | 3.9428 | 2.4871 | 2.2738 | 2.4154 | 6.6356 |
| $\sigma_{01} \times \tau_R$ ($\times 10^{-24}$ cm$^2$ s) | 0.4622 | 1.3336 | 1.1597 | 1.0043 | 1.0233 | 1.4686 |
| $\sigma_{02} \times \tau_R$ ($\times 10^{-24}$ cm$^2$ s) | 1.4368 | 4.4823 | 2.0563 | 1.9809 | 1.7998 | 1.9856 |
| $\sigma_{03} \times \tau_R$ ($\times 10^{-24}$ cm$^2$ s) | 0.1776 | 2.6655 | 0.3659 | 0.2791 | 0.3402 | 3.6243 |

ions turned into positioned at the native defect sites of the ZnS semiconductor. This defect sites serve as non-radiative recombination centers and activate the quenching effect. The factors like ionic difference of $Zn^{2+}$ ions and $Eu^{3+}$ ions, the charge imbalance between the two ions and the higher coordination number of $Eu^{3+}$ in comparison with $Zn^{2+}$ affect the emission properties when $Zn^{2+}$ ions replaced by $Eu^{3+}$ in ZnS lattice. The asymmetry ratio (R), calculated from the ratio of intensity of transitions $^5D_0$-$^7F_2$ to $^5D_0$-$^7F_1$, will give the changes around the $Eu^{3+}$ ions in the system that influence the luminescence property [64].

$$Asymmetric\ ratio(R) = \frac{\int I(5D0 - 7F2)}{\int I(5D0 - 7F1)} \quad (9)$$

The calculated R values under charge transfer bands (CTB) excitation were tabulated in Table 8. The asymmetric ratio greater than 1 indicates the high asymmetric environment around $Eu^{3+}$ ion. The high
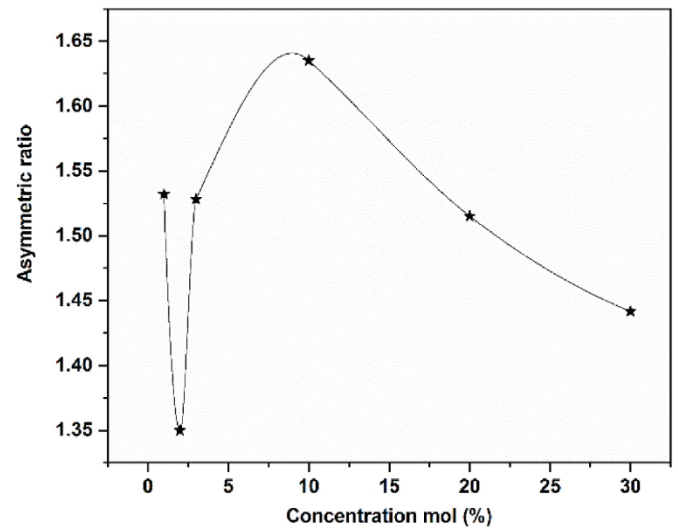


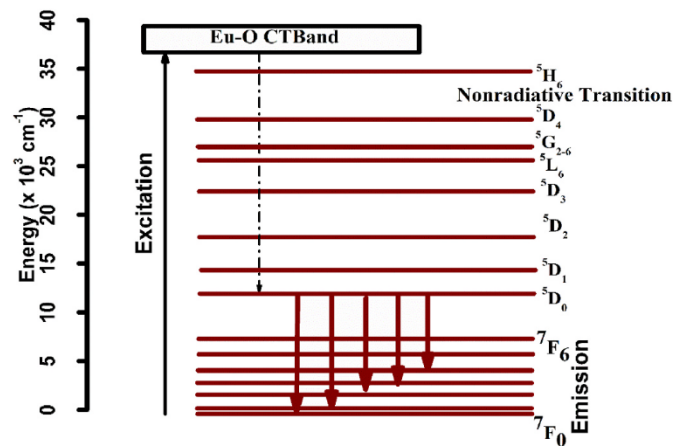**Fig. 13.** Variation of asymmetric ratio of all samples with $Eu^{3+}$ ion concentration.



**Fig. 14.** Partial energy level diagram of ZnS:$Eu^{3+}$ nanophosphors showing the excitation and emission mechanisms.

asymmetric ratio is obtained in the EZS4 sample (10% $Eu^{3+}$ doped ZnS) and it denotes the great asymmetric environment around the metal ion in the material. The dependence of asymmetric ratio with $Eu^{3+}$ concentration is shown Fig. 13.

The energy transfer mechanism from ZnS host to $Eu^{3+}$ ions is shown in Fig. 14. For ZnS: $Eu^{3+}$ nanoparticles, the electrons in the valance band are excited to conduction band after absorbing photons with wavelength 390 nm, an exciton pair is formed. This exciton pair may be trapped by the $Eu^{3+}$ ions and the exciton energy were transferred to $Eu^{3+}$ ion energy levels when the exciton pair moves through the ZnS lattice structure. The photons are emitted and reabsorbed by $Eu^{3+}$ ions. The photon emission is due to the electron-hole recombination and the photon absorption is due to the overlapping of excitation band of $Eu^{3+}$ ion and the band edge emission of ZnS nanoparticles. The $Eu^{3+}$ ions are rapidly relaxed to $^5D_0$ level by multiphonon processes and eventually relaxed to $^7F_J$ (where J = 0 to 6) ground state by characteristic emission radiation. Thus, in ZnS: $Eu^{3+}$ nanophosphors, the ZnS host lattice play a vital role in the luminescence sensitization of $Eu^{3+}$ ions with excitation wavelength 390 nm. The efficient transfer of energy from ZnS host to $Eu^{3+}$ ions illustrates that the $Eu^{3+}$ ions have entered the ZnS host lattice [65]. This efficient energy transfer can be verified by direct pumping and strong emission through the energy levels of $Eu^{3+}$ ions. The sharp lines
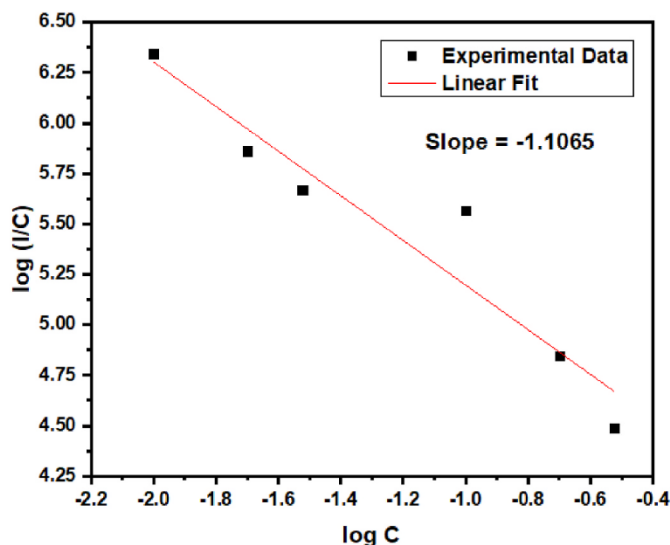
**Fig. 15.** log (I/C) Vs log C plot (Dexter plot).



**Fig. 16.** Temperature dependent photoluminescence (TDPL) spectra of ZnS:0.1Eu$^{3+}$ phosphor.

shown in Fig. 12b are representing the strong energy transfer from ZnS host to Eu$^{3+}$ ions. This can be further confirmed using the excitation spectra shown in Fig.11. That is, the emission from ZnS absorbs Eu$^{3+}$ ions and releases at lower energy. Energy transfer may be better by producing trapping centers and creating energy levels in the ZnS material. When Eu$^{3+}$ ions are doped, it will transfer more anions into the ZnS lattice and decrease the sulfur vacancies level and therefore lower the band emission from the ZnS host matrix [39,66].

In the PL spectra, the peak intensity increased up to concentration x = 0.1 and then decreases. This may be due to the concentration quenching phenomenon of Eu$^{3+}$ ions in ZnS host lattice. According to percolation energy transfer theory, the two main reasons for this concentration quenching effect [67] are (1) the interaction between europium ions that leads to re-absorption of energy by the nearby europium ions and (2) the energy is transferred from the crowd of europium ions to luminescent centers. The energy transfer occurs by an exchange interaction effect or a multipolar exchange interaction. In the case of forbidden transitions, the super exchange interaction effect is responsible for the energy transfer, where the critical distance between neighboring ions is approximately 5 Å. The critical distance (R$_c$) between europium ions can be determined using the formula given by Blasse as [68],

$$R_c \approx 2 \left[ \frac{3V}{4\pi CN} \right]^{1/3} \tag{10}$$

where V = 78.8757 Å is the volume of unit cell in Å, C = 0.1 is the optimum concentration and N = 6 is the number of Zn ion in unit cell. The obtained R$_c$ between Eu$^{3+}$ ions is 6.3096 Å. This value is above 5 Å, so the exchange interaction between Eu$^{3+}$ ions is multipolar exchange. The excitation energy transfer is strongly dependent on the distance between the Eu$^{3+}$ ions. Therefore, in the present case, the calculated critical distance is 6.3096 Å and the mechanism involved is due to multipolar exchange interaction [39]. Therefore, it can be concluded that the concentration quenching occurred in the prepared phosphor material is mainly due to the multipolar interaction between Eu$^{3+}$ ions and not by exchange interaction phenomenon. But the nonradiative multipolar interaction contains dipole-dipole (d-d), dipole-quadrupole (d-q) and quadrupole-quadrupole (q-q) interactions. The exchange interaction confirms using Dexter and Schulman's equation given as [69],
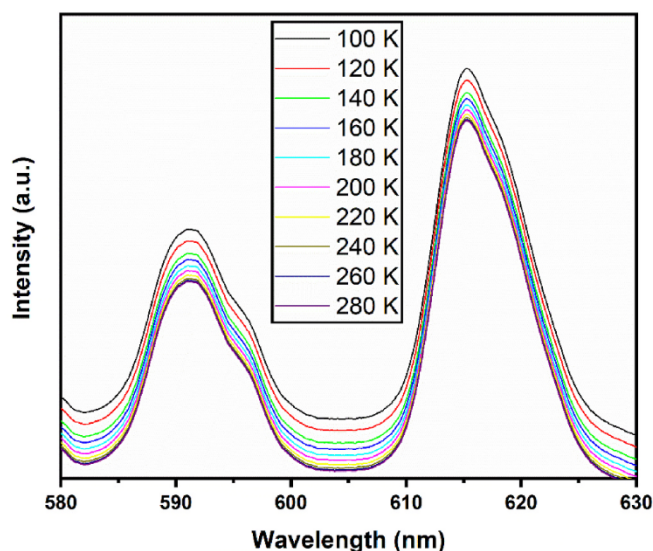
$$\frac{I}{C} = \frac{k}{\beta C^{S/3}} \tag{11}$$

where $\frac{I}{C}$ is the integrated emission intensity per concentration of europium ion in mol %, k and β are constants for each transition and the value of S = 6,8 and 10 corresponds to dipole-dipole (d-d), dipole-quadrupole (d-q) and quadrupole-quadrupole (q-q) interaction, respectively. The Dexter-Schulman's logarithmic plot was shown in Fig. 15. The slope value obtained is 1.1065 and S value is 3.3195. The S value is close to 6, so the type of interaction between Eu$^{3+}$ - Eu$^{3+}$ ions is electric dipole-dipole in nature. The results suggest that the reason for concentration quenching is mainly due to the energy transfer of nearest neighboring Eu$^{3+}$ ions [70].

The energy transfer efficiency ($\eta_{ET}$) in ZnS (sensitizing center) to the Eu$^{3+}$ (luminescent centers) ions can be calculated using the equation [71],

$$\eta_{ET} = 1 - \frac{I}{I_0} \tag{12}$$

where I is the integrated intensities of Eu$^{3+}$ doped ZnS and I$_0$ is the integrated intensities of pure ZnS. The energy transfer efficiency values were calculated from the emission spectra of Eu$^{3+}$ doped ZnS material and tabulated in Table 7. The energy transfer efficiency for 1% Eu$^{3+}$ doped material reaches 22.83%, indicating that it gives the highest energy transfer from ZnS to Eu$^{3+}$ ions. The refractive indices of the prepared materials were determined using Dimitrov – Sakka mathematical relation given by equation (13) and the values were tabulated in Table 7 [72].

$$\frac{n^2 - 1}{n^2 + 2} = 1 - \sqrt{\frac{E_g}{20}} \tag{13}$$

The thermal stability of phosphor materials, which can use in white LEDs, should be investigated as the temperature can affect color stability and emission intensity. The temperature dependent photoluminescence (TDPL) spectra were shown in Fig. 16. From the figure it is clearly seen that the photoluminescence intensity of ZnS: 0.1Eu$^{3+}$ decreases with temperature from 100 K to 280 K and the intensity was decreased small percentage of the initial intensity even at 280 K. The figure indicated that the photoluminescence intensity of ZnS: 0.1Eu$^{3+}$ decreases slightly as temperature changes from 100 K to 280 K. There is only a small percentage change in the initial intensity even at 280 K. There is no thermal quenching behavior present in the material indicating the outstanding thermal stability of the prepared phosphor [73].

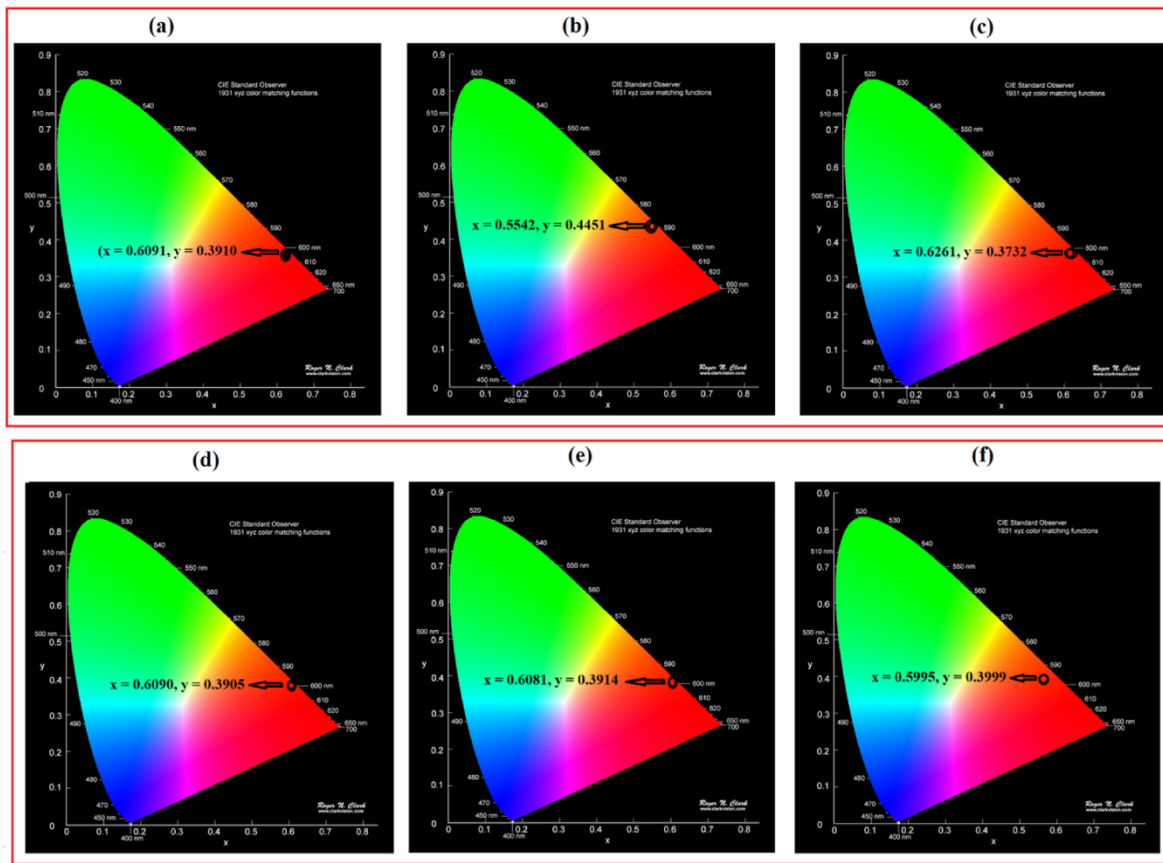The Commission International de L'Eclairage (CIE) in 1931 proposed

**Fig. 17.** (a), (b), (c), (d), (e) & (f). CIE chromaticity diagram of $Zn_{(1-x)}S:xEu^{3+}$ (x = 0.01, 0.02, 0.03, 0.1, 0.2 & 0.3) phosphor.

a collection of three matching functions $\bar{x}(\lambda)$, $\bar{y}(\lambda)$ and $\bar{z}(\lambda)$ comparable with red, green and blue to the production of monochromatic colors with wide range. This color matching functions can be expressed in the 2D plane, gives the color chromaticity diagram. The color can be defined by the chromaticity coordinates (x,y) explained by Ref. [74]:

$$x = \frac{X}{X+Y+Z} \tag{14}$$

$$y = \frac{Y}{X+Y+Z} \tag{15}$$

The CIE (x,y) chromaticity diagram using chromaticity coordinates (x,y) is shown in Fig. 17. The CIE color chromaticity coordinates obtained from the emission spectra of all the samples were listed in Table 7. The CIE coordinate of all the samples were almost same and close to the standard red color region of the CIE diagram. The corresponding calculated color temperature (CCT), measured in Kelvin (K) has been evaluated using McCamy's method [75] for knowing the color emission performance. The McCamy's approximation is given by:

$$CCT = -449\,n^3 + 3525\,n^2 - 6823.3\,n + 5520.33 \tag{16}$$

where $n = \frac{(x-x_e)}{(y-y_e)}$ and $x_e = 0.3320$, $y_e = 0.1858$ are the epicentre of convergence. The low CCT values are related with cool red light region which is in agreement with chromaticity coordinates. The color purity of the prepared phosphor can be calculated using Fred Schubert concept and is given by Ref. [74]:

$$Color\ Purity = \frac{\sqrt{(x_s - x_i)^2 + (y_s - y_i)^2}}{\sqrt{(x_d - x_i)^2 + (y_d - y_i)^2}} \times 100\ \% \tag{17}$$

where $(x_i,y_i)$ is the CIE coordinates of white illuminant point, $(x_s,y_s)$ is

the CIE coordinates of the sample point and $(x_d,y_d)$ are the coordinates comparable to dominant wavelength (DW) of emission. The calculated CCT values and the color purity of all the phosphor samples were listed in Table 7. These two parameters are the main indicators for evaluating the phosphor's performance. Generally, the CIE (x, y) coordinates of the standard red phosphor lies in the range x = 0.670 and y = 0.330. For $0.03Eu^{3+}$: ZnS phosphors, the CIE color coordinate, the dominant wavelength and the CCT value were (x = 0.6261, y = 0.3732), (0.63, 0.37) and 1758.39 K respectively. The color purity of $0.03Eu^{3+}$: ZnS material was found to be 0.9884. The high color purity value indicates that the red light emission from the prepared phosphor sample is close to the standard red light source. The observed photoluminescence spectra with great color purity indicate that the $0.03Eu^{3+}$: ZnS is a potential candidate for red light generation. Generally, the photoluminescence decay time depends on the luminescence centers, lattice imperfection, energy transfer and doping in the host lattice. The exponential decay behavior of $ZnS/Eu^{3+}$ material was performed to know the site occupancy details of the system. The $^5D_0$-$^7F_2$ transition at 614 nm can be used for analyzing the life time decay experiment with excitation wavelength 390 nm and is shown in Fig. 18. The experimental decay time fitted with exponential of first order function is given by the following relation [76].

$$I(t) = I_0 \exp\left(-\frac{t}{\tau}\right) \tag{18}$$

where $I_o$ is the initial intensity of emission at t = 0 and $\tau$ is the emission life time. The life time obtained from the results was confirmed with the reported values of $Eu^{3+}$ doped ZnS nanophosphor system. The life time is found to be decreasing with concentration due to the faster decay rates. The increasing rate of non radiative transitions of activator ions allows for rapid decay and thus shortening of life time. From the results,
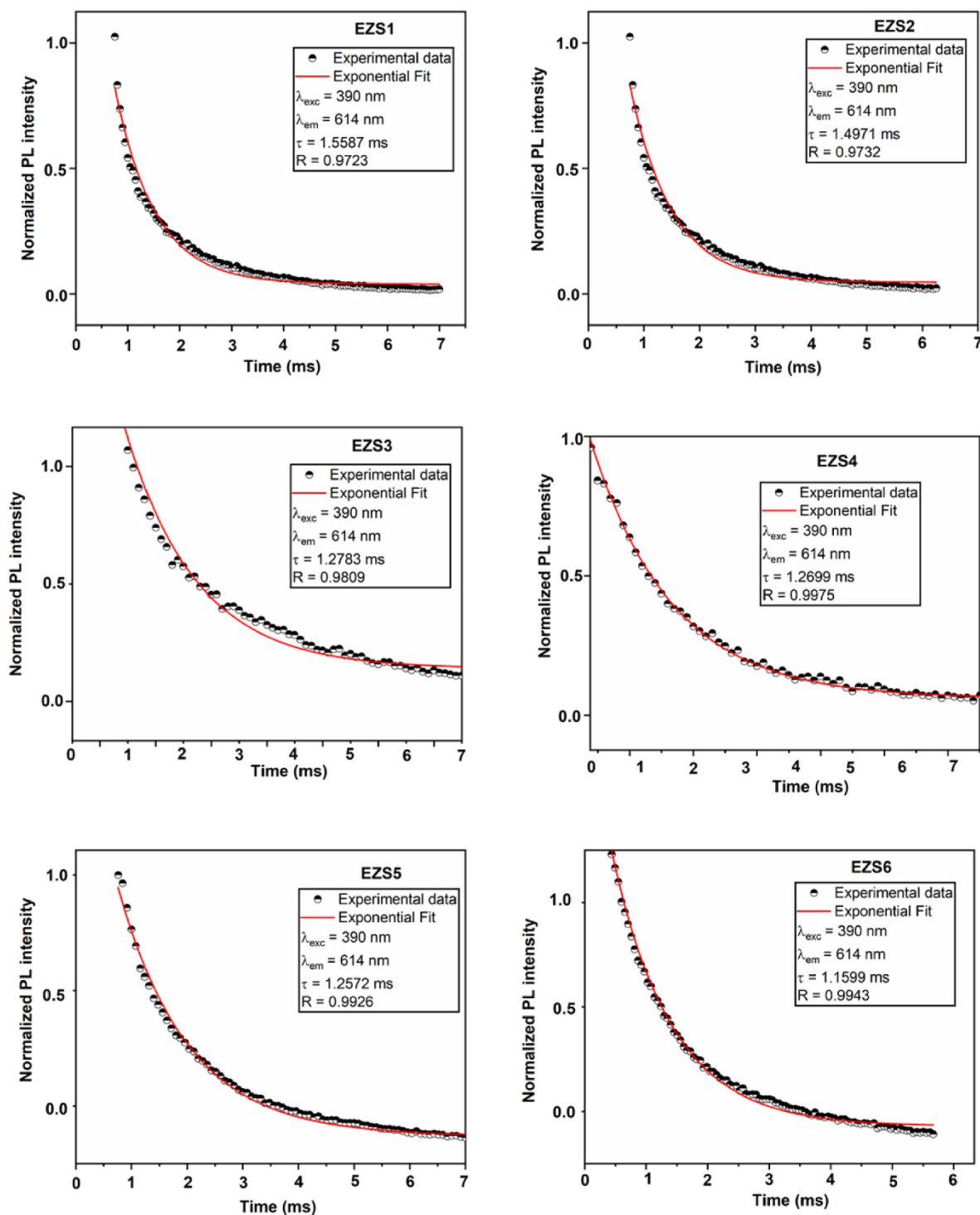
**Fig. 18.** Room temperature luminescent decay curves of $^5D_0$-$^7F_2$ transition at 614 nm for $Eu^{3+}$ ions in all the samples.

we can conclude that $Eu^{3+}$ was occupied in a single site and decay time varies with doping. There is a difference in the calculated life time obtained from Judd-Ofelt theory and experimentally observed value. This difference is due to the multiphonon relaxation rates ($W_{NR}$) of excited $Eu^{3+}$ ions, which is given by,

$$W_{NR} = \frac{1}{\tau_{exp}} - \frac{1}{\tau_{cal}} \quad (19)$$

The muliphonon relaxation rate calculated for $Zn_{0.9}S$: $Eu^{3+}$ is 0.2642 ms and it is low compared with other samples which are tabulated in

Table 8. The results show reduced life time as a result of high multiphonon relaxation rates of excited $Eu^{3+}$ ions.

The Judd-Ofelt theory (J-O) is used to describe the transition intensity of rare earth ions in material environments. The Judd-Ofelt parameters $\Omega_\lambda$ ($\lambda = 2$, 4 and 6) calculated were used to determine the local structural changes and the bonding around the $Eu^{3+}$ ion due to the variation in doping. This theory gives idea about oscillator strengths, life time decay, emission probabilities, quantum efficiency etc [77]. In the case of $Eu^{3+}$ ion, the magnetic dipole transition ($^5D_0$-$^7F_1$) gives the intensity parameters from the photoluminescence spectra which are

considered as a reference. In this work, the J-O and other radiative parameters were calculated from the emission spectra. According to the J-O theory, the MD transition rate ($A_{01}$) of $^5D_0$-$^7F_1$ transition of $Eu^{3+}$ ion is given from the following equation:

$$A_{01} = \frac{64\pi^4 \nu_1^3 n^3 S_{md}}{3h\,(2J+1)} \quad (20)$$

The ED transition rate ($A_{0J}$) of $^5D_0$-$^7F_J$ transition (J = 2, 4 and 6) is defined as:

$$A_{0J} = \frac{64\pi^4 \nu_J^3}{3h(2J+1)} e^2 \frac{n(n^2+2)^2}{9} \sum_{\lambda=2,4,6} \Omega\lambda \left|\langle^5D_0\|U^{(\lambda)}\|^7F_J\rangle\right|^2 \quad (21)$$

where $A_{0J}$ is the experimental coefficient of spontaneous emission, h is the Planck's constant = $6.626 \times 10^{-34}$ Js or $4.135 \times 10^{-15}$ eVs, e is the charge of electron, $\nu_J$ is the wavenumber of the corresponding transition, n is the refractive index, $2J+1$ is the first degenerated state which is equal to 1 for $^5D_0$ transitions, $S_{md}$ is the strength of the MD transition which is equal to $9.6 \times 10^{-42}$ units and $\Omega_\lambda$ are called the JO parameters, $\left|\langle^5D_0\|U^{(\lambda)}\|^7F_J\rangle\right|^2$ is the unit tensor doubly reduced matrix element whose values are independent of chemical surroundings of the ion and are 0.00324, 0.00229 and 0.00023 for J = 2, 4 and 6 respectively. Hence, $\Omega_2$, $\Omega_4$ and $\Omega_6$ can be estimated. In this work, $\Omega_6$ cannot be calculated since the $^5D_0$-$^7F_6$ transition emission falls on the infrared region and it was too weak to be detected through experimentally. The parameter $\Omega_2$ greatly affects the site occupy by $Eu^{3+}$ ion and the parameter $\Omega_4$ gives the details about the stability and rigidity of the host material. The JO intensity parameter of $Zn_{0.9}S{:}0.1Eu^{3+}$ is $\Omega_2 = 2.0412 \times 10^{-22}$ cm$^2$ and $\Omega_4 = 0.4207 \times 10^{-22}$ cm$^2$. The high value of $\Omega_2$ compared with $\Omega_4$ of all the doped samples evidenced high symmetry of site occupied by $Eu^{3+}$ ion. In this work, $\Omega_2 > \Omega_4$ is the trend observed in all the $Eu^{3+}$ doped samples.

The relation connecting observed life time ($\tau_{obs}$), radiative transition rate ($A_R$) and non-radiative transition rate ($A_{NR}$) can be defined as:

$$\frac{1}{\tau_{obs}} = A_R + A_{NR} \quad (22)$$

The total radiative emission probability ($A_R$) can be defined as sum of all radiative transition rates $A_{0J}$ and is given by:

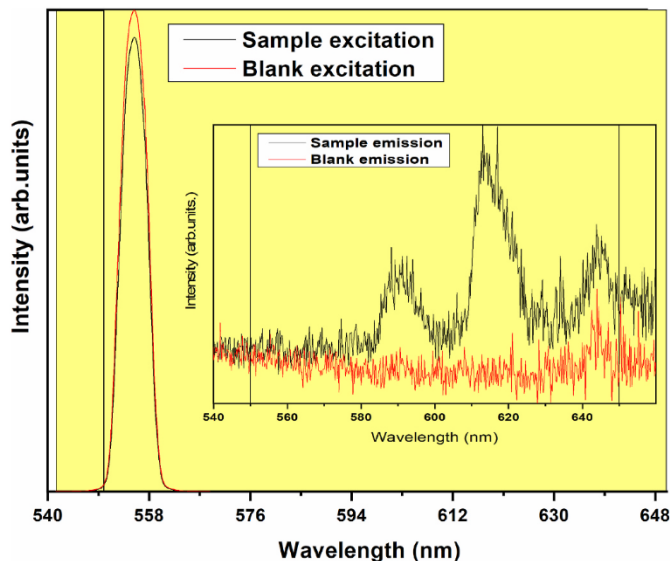$$A_R = \sum_{J=0}^{4} A_{0J} \quad (23)$$



**Fig. 19.** Quantum yield measurement made using integrating sphere.

The reciprocal of coefficients for spontaneous emission $\sum A_{0J}$ is equal to the radiative fluorescence life time ($\tau_{rad}$), given by:

$$\tau_{rad} = \frac{1}{\sum A_{0J}} = \frac{1}{A_R} \quad (24)$$

Further, the emission internal quantum efficiency ($\eta_{int}$) can be calculated using measured life time ($\tau_{obs}$) and calculated radiative lifetime ($\tau_{rad}$) and is given as the ratio between the numbers of photons emitted by the $Eu^{3+}$ ion to that of photons absorbed.

$$\eta_{int} = \frac{\tau_{obs}}{\tau_{rad}} = \frac{A_R}{A_R + A_{NR}} \quad (25)$$

The external quantum efficiency ($\eta_{ext}$) of the prepared phosphor is obtained from the emission spectra and is given as the ratio of number of photons in the emission spectra to the excitation spectra of the material [78].

$$\eta_{ext} = \frac{\int \lambda P(\lambda)d\lambda}{\int \lambda E(\lambda)d\lambda} \quad (26)$$

where $\frac{P(\lambda)}{h\nu}d\lambda$ and $\frac{E(\lambda)}{h\nu}d\lambda$ are defined as the number of photons in the emission and excitation region of the material respectively. The internal and external quantum efficiencies of the prepared phosphors are given in Table 8. The fluorescence branching ratio ($\beta_{0J}$) measures the emission input of each transition from a state to all final transition state. The $\beta_{0J}$ is calculated by the following relation:

$$\beta_{0J} = \frac{A_{0J}}{\sum A_{0J}} \quad (27)$$

where $J = 1$, 2 and 4. The highest branching ratios of all the samples were found for $^5D_0$-$^7F_2$ transition which has the highest dominant emission peak at red line. The stimulated emission cross-section ($\sigma_{0J}$) of $^5D_0 \rightarrow ^7F_J$ can be calculated as:

$$\sigma_{0J} = \frac{\lambda_p^4}{8\pi c n^2 \Delta\lambda_{eff}} A_{0J} \quad (28)$$

where $\lambda_p$ is the wavelength of peak emission transition, $\Delta\lambda_{eff}$ is the effective line width of the emission peak or FWHM wavelength of transition and c is the velocity of light. The highest stimulated emission cross section ($\sigma_{02}$) for all the samples obtained for $^5D_0$-$^7F_2$ electronic transition illustrates that it is the most ultimate powerful transition.

The radiative emission probability ($A_R$), Radiative fluorescence life time ($\tau_{rad}$) and Observe life time ($\tau_{obs}$), quantum efficiency ($\eta$), fluorescence branching ratio ($\beta_{0J}$) and stimulated emission cross-section ($\sigma_{0J}$) for all the samples were calculated using above equations and tabulated in Table 8. The EZS4 material has more internal and external quantum efficiencies as 66.97% and 34.31%. For all the samples, the red emission ($^5D_0$-$^7F_2$) transition has maximum branching ratios and color purity. The stimulated emission cross-section ($\sigma_{0J}$) results were used to estimate the emission transition characteristics of $Eu^{3+}$ ion into the ZnS material. The $\sigma_{01}$ and $\sigma_{02}$ values are maximum for EZS4 material and $\sigma_{03}$ value is maximum for EZS6 material. The high value of stimulated emission cross-section, $10.365 \times 10^{-20}$ cm$^2$ for $^5D_0$-$^7F_2$ transition, indicates that the material has good optical transition behavior [79]. The gain width and the optical gain together give the idea about the internal intensity of light and incorporation of europium ion into the ZnS lattice. It is the most important property showing the maximum or minimum output power. The high value of gain bandwidth was due to $^5D_0$-$^7F_2$ transition for ESZ4 material and its value is $9.6775 \times 10^{-28}$ cm$^3$. The high optical gain shows that the materials are having good semiconductor optical amplifier. The gain bandwidth and optical gain values of all the samples were presented in Table 8. Shortly, the incorporation of $Eu^{3+}$ ion in ZnS host lattice affects the luminescence intensity of the prepared phosphor materials. The values obtained were comparable with the literature reported values and the results suggest that $0.1Eu^{3+}$:

**Table 9**
Overview of peak emission wavelength and quantum yield of different red phosphors and commercial red phosphors.

| Red phosphor | Peak emission wavelength (nm) | Quantum Yield (%) | References |
|---|---|---|---|
| $Y_2O_2S$: $Eu^{3+}$ | 628 | 4.2 | [71] |
| ZnS/$Eu^{3+}$ | 620 | $(0.27 \pm 0.02)$ | [79] |
| ZnS–SHIL–Eu(TAA)$_4$ (Hybrid material) | 614 | 2.49 | [74] |
| CdS–SHIL–Eu(TAA)$_4$ (Hybrid material) | 614 | 4.22 | [74] |
| Anthracene (Rare-earth-free Phosphors) | 681 | 3 | [72] |
| $TiO_2$: $Eu^{3+}$ | 612 | 0.03 | [76] |
| $La_2O_2S$ (Yb,Ho) | 756 | 0.12 | [77] |
| Commercial red phosphor (Red nitride) | 629 | $0.89 \pm 0.04$ | [80] |
| ZnS: $Eu^{3+}$ | 614 | $2.54 \pm 0.46$ | This work |

ZnS is an excellent material for semiconductor optical amplifier.

Quantum Yield.

The luminescence quantum efficiency is calculated using the theoretical ($\tau_{rad}$) and experimental values ($\tau_{obs}$) of life times attained from the $^5D_0$ level.

$$\eta = \frac{\tau_{obs}}{\tau_{rad}} \tag{29}$$

The quantum efficiency obtained is 66.97% for optimum concentration of $Eu^{3+}$. The internal quantum efficiency ($\eta_{IQE}$) of ZnS:0.1$Eu^{3+}$ phosphor was resolved with the help of integrating sphere method as shown in Fig. 19. The experimental internal quantum yield of high fluorescence intensity material is $(2.54 \pm 0.46)$ % which is higher than that of reported values of ZnS/$Eu^{3+}$ $(0.27 \pm 0.02)$ in the literature [22]. ZnS/$Eu^{3+}$ material has longer life time and lower quantum yield compared with other luminescent materials. This is due to the difference in the energy transfer mechanism present in the material. There are so many factors affecting the luminescence quantum yields. The quantum yields of different red phosphors are shown in Table 9. However, the quantum yields of ZnS: $Eu^{3+}$ is relatively low, it is better than commercially available red phosphor used for LED applications as shown in table.

## 4. Conclusions

A series of $Zn_{(1-x)}S$:$x$$Eu^{3+}$ semiconductor phosphors were synthesized by the low temperature conventional solid state reaction method. The average crystallite size calculated using Debye Scherrer method and Size-Strain Plot method were found to be comparable and the small value of lattice strain illustrate a small distortion happened in the host lattice due to the incorporation of $Eu^{3+}$ ions. The optical band gap energy suggested that the prepared phosphor can act as host matrices for luminescence centers. The high fluorescence intensity is obtained for $Zn_{0.9}S$:0.1$Eu^{3+}$ which is identified to be the optimum. All the prepared phosphors exhibit intense red emission having comparable ($x$,$y$) coordinates with standard phosphor $x = 0.670$ and $y = 0.330$. The trend $\Omega_2 > \Omega_4$ (JO intensity parameters) present in all the samples revealed the high symmetry occupied by $Eu^{3+}$ ions. The decay curves were single exponentially fitted and the life time is found to be decreasing with concentration due to the faster decay rates. The prepared phosphors have better radiative characteristics including branching ratio and emission cross section. These experimental results indicated the potential application of the prepared red phosphor in the field of designing various optoelectronic devices.

## Credit author statement

**Jincemon Cyriac:** Investigation, Software. **Deepthi N Rajendran:**

Conceptualization, Resources, Supervision. **L.S. Archana:** Methodology, Investigation, Writing - Original Draft, Writing - Review & Editing, Validation, Formal analysis, Data curation, Visualization.

## Declaration of competing interest

The authors declare that they have no known competing financial interests or personal relationships that could have appeared to influence the work reported in this paper.

## References

[1] T. Krishnapriya, et al., An insight into the luminescent properties and Judd– Ofelt analysis of $Eu^{3+}$ doped $CaZn_2(PO4)_2$ phosphors, J. Mater. Sci. Mater. Electron. (2020), https://doi.org/10.1007/s10854-020-04746-0.
[2] Jingzhi Fang, et al., Recent Advances in Low-dimensional Semiconductor Nanomaterials and Their Applications in High-performance Photodetectors, Wiley Online Library, 2019, https://doi.org/10.1002/inf2.12067.
[3] A. Peter, Ajibade et al, Synthesis and Characterization of metal Sulfides nanoparticles/Poly (methyl methacrylate) nanocomposites, Int. J. Polymer Sci. (2014), https://doi.org/10.1155/2014/752394.
[4] Shinkichi Tanimizu, Principal Phosphor Materials and Their Optical Properties, Fundamentals of Phosphors, Book Chapter, 2006, https://doi.org/10.1201/9781420043686.ch2.
[5] Jaya Dwivedi, et al., A commercial approach for the fabrication of bulk and nano phosphors converted into highly efficient white LEDs, RSC Adv. 4 (2014) 54936–54947, https://doi.org/10.1039/C4RA11318G [15].
[6] P. D'Amico, et al., New energy with ZnS: novel applications for a standard transparent compound, Sci. Rep. 7 (2017) 16805, https://doi.org/10.1038/s41598-017-17156-w.
[7] S. John, McCloy et al, Physics and Chemistry of ZnS, Book Chapter: Chemical Vapour Deposited Zinc Sulfide, 2013, 10.1117/3.1001953.ch1.
[8] S.B. Qadri, et al., The effect of particle size on the structural transitions in Zinc Sulfide, J. Appl. Phys. 89 (2001) 115–119.
[9] Raheel Januja, et al., $Na^+$ driven nucleation of $NaYF_4$: Yb, Er nanocystals and effect of temperature on their structural transformations and luminescent properties, J. Phys. Chem. C 122 (2018) 40, https://doi.org/10.1021/acs.jpcc.8b09327.
[10] Pai Chia Kuo, et al., Synthesis and photoluminescent properties of wurtzite ZnS nanorods by hydrothermal and Co-precipitation methods, J. Ceram. Soc. Jpn. 114 (11) (2006) 918–922.
[11] Selishchev, et al., Luminescence and spectral characteristics of zinc sulfide nanoparticles doped with $Eu^{2+}$, Theor. Exp. Chem. 51 (2016) 366–374, https://doi.org/10.1007/s11237-016-9437-y.
[12] A. Kumar, et al., Enhancing the photoluminescence of ferroelectric liquid crystal by doping with ZnS quantum dots, Appl. Phys. Lett. 100 (2012) 134101, https://doi.org/10.1063/1.3698120.
[13] Md Anisuzzaman Shakil, et al., A Review on zinc sulphide thin film fabrication for various applications based on doping elements, Mater. Sci. Appl. 9 (9) (2018) 751–778, https://doi.org/10.4236/msa.2018.99055.
[14] K. Ashwini, et al., Synthesis and optical properties of undoped and Eu-doped ZnS nanoparticles, Phys. Scripta 85 (6) (2012), https://doi.org/10.1088/0031-8949/85/06/065706.
[15] Sabit Horoz, et al., Controlled synthesis of $Eu^{2+}$ and $Eu^{3+}$ doped ZnS quantum dots and their photovoltaic and magnetic properties, AIP Adv. 6 (2016) 45119, https://doi.org/10.1063/1.4948510.
[16] Liping wang, et al., Preparation and photoluminescent properties of doped nanoparticles of ZnS by solid-state reaction, J. Lumin. 130 (1) (2010) 137–140, https://doi.org/10.1016/j.jlumin.2009.07.036.
[17] Chun-Hua Yan, et al., $Eu^{3+}$ion as fluorescent probe for detecting the surface effect in naocrystals, Appl. Phys. Lett. 82 (20) (2003) 3511–3513, https://doi.org/10.1063/1.1575504.

[18] M. Mateus, Ferrer et al, Europium doped zinc sulfide: a correlation between experimental and theoretical calculations, J. Mol. Model. 20 (2014) 2375, https://doi.org/10.1007/s00894-014-2375-5.

[19] Gurmeet Singh Lotey, et al., Structural and photoluminescence properties of Eu-doped ZnS nanoparticles, Mater. Sci. Semicond. Process. 16 (6) (December 2013) 2044–2050, https://doi.org/10.1016/j.mssp.2013.07.039.

[20] Alexander Ciric, et al., Judd-Ofelt parametrization from emission spectra: the case study of the Eu$^{3+}$ $^5D_1$ emitting level, Chem. Phys. 528 (2020) 110513.

[21] Yongbo Wang, et al., Incorporation of lanthanide (Eu$^{3+}$) ions in ZnS semiconductor quantum dots with a trapped-dopant model and their photoluminescence spectroscopy study, IOP Pub. nanotechnol. 26 (8pp) (2015) 375601.

[22] L.S. Archana, et al., Structural and Optical properties of Ce$^{3+}$doped ZnS nanoparticles, Adv. Sci. Lett. 24 (2018) 5994–5999, https://doi.org/10.1166/asl.2018.12233.

[23] Prabeer Barpanda, et al., Structure and Electrochemical Properties of Novel Mixed Li(Fe$_{1-x}$M$_x$)SO$_4$F (M=Co, Ni, Mn) Phases Fabricated by Low Temperature Ionothermal Synthesis, Royal Society of Chemistry, 2010.

[24] t al Zhou Jian, The physical meanings of 5 basic parameters for an X-ray diffraction peak and their application, Chin. J. Geochem. 22 (1) (2003), https://doi.org/10.1007/BF02831544.

[25] Sefako J Mofokeng, et al., Structural, optical and photoluminescence properties of Eu$^{3+}$ doped ZnO nanoparticles, Spectrochim. Acta Part A Molecular and Biomolecular Spectroscopy 182 (2017) 42–49.

[26] P. Bindu, et al., Estimation of lattice strain in ZnO nanoparticles: X-ray peak profile analysis, J. theoretical Appl. Phys. 8 (2014) 123–134, https://doi.org/10.1007/S40094-014-0141-9.

[27] B.D. Cullity, Elements of X-Ray Diffractions, Addison-Wesley, 1956.

[29] L.S. Archana, et al., Luminescence of rare earth doped ZnS nanophosphors for the applications in optical displays, Mater. Today Proc. (2020), https://doi.org/10.1016/j.matpr.2020.05.227.

[30] Medha Bhushan, et al., Reduced band gap and diffusion controlled spherical n-type ZnS nanoparticles for absorption of UV-Vis region of solar spectrum, J. Phys. Chem. Solid. 135 (2019), https://doi.org/10.1016/j.jpcs.2019.05.018, 109021.

[31] Tianyou Zhai, et al., Vapor-phase synthesis of one-dimensional ZnS, CdS and Zn$_x$Cd$_{1-x}$S nanostructures, Pure Appl. Chem. 82 (11) (2010) 2027–2053, https://doi.org/10.1351/PAC-CON-09-09-18.

[32] K. Maniammal, et al., X-ray diffraction line profile analysis of nanostructured nickel oxide: shape factor and convolution of crystallite size and microstrain contributions, Physics 85 (2017) 214–222, https://doi.org/10.1016/j.physe.2016.08.035.

[33] A. Khorsand Zak, et al., X-ray analysis of ZnO nanoparticles by Williamson-Hall and size-strain plot methods, Solid State Sci. 13 (1) (January 2011) 251–256.

[34] P. Bindu, et al., Estimation of lattice strain in ZnO nanoparticles: X-ray peak profile analysis, J. Theoretical Appl. Phys. 8 (2014) 123–134.

[35] Yendrapati Taraka Prabhu, et al., X-ray analysis by Williamson- Hall and Size-strain plot methods of ZnO nanoparticles with fuel variation, World J. Nano Sci. Eng. 4 (2014) 21–28.

[36] Rahizana Mohd Ibrahim, et al., Optical properties of Ni$^{2+}$, Co$^{2+}$, and Mn$^{2+}$ doped ZnS nanoparticles synthesized using reverse Micelle method, ECS J. Solid State Sci. technol. 4 (2) (2015) R31–R37, https://doi.org/10.1149/2.0181502jss.

[37] G. Janita Christobel, Vibrational spectroscopy of ZnO-ZnS nanoparticles, Int. J. Sci. Res. 5 (6) (June 2016), https://doi.org/10.21275/v5i6.NOV164755.

[38] Jincemon Cyriac, et al., Dysprosium-substitution-induced structural changes of multiferroic nanocrystalline bismuth ferrite and the investigation through positron annihilation and other studies, Physica B: Phys. Condens. Matter (2020), https://doi.org/10.1016/j.physb.2020.412431.

[39] Sucheta Juneja, et al., Effect of power on crystallinity and opto-electronic properties of silicon thin films grown using VHF PECVD process, Silicon (2020), https://doi.org/10.1007/s12633-020-00697-7.

[40] L.S. Archana, et al., An insight into the structure, luminescent characteristics and Judd-Ofelt analysis of (1-x) ZnS-(x) Dy$_2$O$_3$ phosphors, Mater. Sci. Semicond. Process. 128 (2021) 105752, https://doi.org/10.1016/j.mssp.2021.105752.

[41] Piyal Maity, et al., Selective near-infrared (NIR) photodetectorsfabricated with colloidal CdS:Co quantum dots, J. Mater. Chem. C 7 (2019) 7725–7733, https://doi.org/10.1039/c9tc01871a.

[42] Stanislav I. Sadovnikov, et al., Synthesis and optical properties of nanostructured ZnS and heteronanostructures based on zinc and silver sulfides, J. Alloys Compd. 831 (2020), https://doi.org/10.1016/j.jallcom.2020.154846, 154846.

[43] P.E. Agbo, et al., Analysis on energy bandgap of Zinc Sulphide (ZnS) thin films grown by solution growth technique, Chalcogenide Lett. 14 (8) (August 2017) 357–363.

[44] Mou Pal, et al., Synthesis of Eu$^{3+}$ doped ZnS nanoparticles by a wet chemical route and its characterization, Opt. Mater. 35 (12) (2013) 2664–2669, https://doi.org/10.1016/j.optmat.2013.08.003.

[45] Zhiren Wei, et al., Synthesis and luminescent modulation of ZnS crystallite by a hydrothermal method, ACS Omega 3 (1) (2018) 137–143, https://doi.org/10.1021/acsomega.7b01574.

[46] Yeong Hwan Ko, Luminescence properties of europium ions-doped yttrium silicate (Y$_2$SiO$_5$:Eu$^{3+}$) nanocrystalline phosphors: effect of Eu$^{3+}$ ion concentration and thermal annealing, J. Nanosci. Nanotechnol. 13 (5) (2013) 3230–3235, https://doi.org/10.1166/jnn.2013.7144.

[47] Ying Mei, Ye Lu and Bing Yan Soft hybrids of Eu$^{3+}$ beta-diketonates and MS (M = Zn, Cd) nanoparticles using mercapto-ionic liquid linkage for white luminescence integration, s, New J. Chem. 37 (2013) 2619, https://doi.org/10.1039/c3nj00547j.

[48] Ishwar Prasad Sahu, et al., Studies on the luminescence properties of CaZrO$_3$:Eu$^{3+}$ phosphors prepared by the solid state reaction method, J. Sci.: Adv. Mater. Devices (2017), https://doi.org/10.1016/j.jsamd.2017.01.00.

[49] Yiyu Li, et al., Green phosphorescence of zinc sulfide optical ceramics, Opt. Mater. Express 4 (6) (2014), https://doi.org/10.1364/OME.4.001140.

[50] Neslihan Uzar, Synthesis and investigation of optical properties of ZnS nanostructures, Bull. Mater. Sci. 34 (2) (April 2011) 287–292, https://doi.org/10.1007/s12034-011-0085-5.

[51] Santosh K. Gupta, Eu$^{3+}$ local site analysis and emission characteristics of novel Nd$_2$Zr$_2$O$_7$:Eu phosphor: insight into the effect of europium concentration on its photoluminescence properties, RSC Adv. 6 (2016) 53614–53624, https://doi.org/10.1039/C6RA11698A.

[52] I. Ahemen, et al., White light tunable emissions from ZnS: Eu$^{3+}$ nanophosphors over 330–465 nm excitation range for white LED applications, Mater. Res. Express 3 (4) (2016), https://doi.org/10.1088/2053-1591/3/4/045016.

[53] Iorkyaa Ahemen, Synthesis and characterization of europium-doped zinc sulphide (ZnS:Eu) nano particles: nano red phosphor, Adv. Sci. Eng. Med. 5 (11) (2013) 1188–1194, https://doi.org/10.1166/asem.2013.1403.

[54] Yongbo Wang, et al., Incorporation of lanthanide (Eu$^{(3+)}$) ions in ZnS semiconductor quantum dots with a trapped-dopant model and their photoluminescence spectroscopy study, Nanotechnology 26 (2015) 375601, https://doi.org/10.1088/0957-4484/26/37/375601.

[55] Gurmeet Singh Lotey, et al., Structural and photoluminescence properties of Eu-doped ZnS nanoparticles, Mater. Sci. Semicond. Process. 16 (6) (December 2013) 2044–2050, https://doi.org/10.1016/j.mssp.2013.07.039.

[56] Sabit Horoz, Controlled synthesis of Eu$^{2+}$ and Eu$^{3+}$ doped ZnS quantum dots and their photovoltaic and magnetic properties, AIP Adv. 6 (2016) 45119, https://doi.org/10.1063/1.4948510.

[57] Lun Ma, et al., A violet emission in ZnS:Mn,Eu: luminescence and applications for radiation detection, J. Appl. Phys. 115 (2014), 1031042014, https://doi.org/10.1063/1.4868221.

[59] Koen Binnemans, Interpretation of europium(III) spectra, Coord. Chem. Rev. 295 (1 July 2015) 1–45, https://doi.org/10.1016/j.ccr.2015.02.015.

[60] Eugenio Cantelar, et al., Structural, photoluminescent properties and Judd-Ofelt analysis of Eu$^{3+}$-activated CaF$_2$ nanocubes, J. Alloys Compd. 813 (15 January 2020) 152194, https://doi.org/10.1016/j.jallcom.2019.152194.

[61] Xiuli Wang, Visible emission characteristics from different defects of ZnS nanocrystals, Phys. Chem. Chem. Phys. 13 (2011) 4715–4723, https://doi.org/10.1039/C0CP01620A.

[62] Yongbo Wang, Incorporation of lanthanide (Eu$^{(3+)}$) ions in ZnS semiconductor quantum dots with a trapped-dopant model and their photoluminescence spectroscopy study, Nanotechnology 26 (37) (2015) 375601, https://doi.org/10.1088/0957-4484/26/37/375601.

[63] Prasun Mukherjee, et al., Lanthanide sensitization in II–VI semiconductor materials: a case study with terbium (III) and europium (III) in zinc sulfide nanoparticles, J. Phys. Chem. 115 (16) (2011 Apr 28) 4031–4041, https://doi.org/10.1021/jp109786w.

[64] G. Jyothi, et al., Site selective substitution and its influence on photoluminescence properties of Sr$_{0.8}$Li$_{0.2}$Ti$_{0.8}$Nb$_{0.2}$O$_3$:Eu$^{3+}$ phosphors, RSC Adv. 7 (2017) 28438–28451, https://doi.org/10.1039/C7RA04351A.

[65] P.M. Tan, et al., New sights on the energy transfer mechanisms of Eu-doped CdS quantum dots, Phys. Chem. Chem. Phys, Royal society of Chemistry (2020).

[66] Weiyi Jia, et al., Energy transfer from the host to Eu$^{3+}$ in ZnO, Opt. Mater. 23 (2003) 27–32, https://doi.org/10.1016/S0925-3467(03)00054-5.

[67] Zijun Wang, et al., Concentration quenching in upconversion nanocrystals, J. Phys. Chem. C 122 (45) (2018) 26298–26306, https://doi.org/10.1021/acs.jpcc.8b09371.

[68] Yan Zhang, et al., Luminescence properties and energy migration mechanism of Eu$^{3+}$ activated Bi$_4$Si$_3$O$_{12}$ as a potential phosphor for white LEDs, Mater. Res. Express 5 (2018) 26202, https://doi.org/10.1088/2053-1591/aaab8a.

[69] Kanchan Mondal, et al., Investigation of photoluminescence properties, thermal stability, energy transfer mechanisms and quantum efficiency of Ca$_2$ZnSi$_2$O$_7$: Dy$^{3+}$, Eu$^{3+}$ phosphors, J. Lumin. 195 (2018) 259–270, https://doi.org/10.1016/j.jlumin.2017.11.028.

[70] M. Ayvacikli, et al., Cathodoluminescence and photoluminescence properties of Dy doped La$_2$CaB$_{10}$O19 phosphor, Opt. Mater. 110 (2020) 110531, https://doi.org/10.1016/j.optmat.2020.110531.

[71] S. Som, P. Mitra, V. Kumar, V. Kumar, J. Terblans, H. C Swart, S. K Sharma, Dalton Trans. 43 (2014) 9860–9871.

[72] Rachod Boonsin, Genevieève Chadeyron, Jean-Philippe Roblin, Damien Boyer and Rachid Mahiou, Development of rare-earth-free phosphors for eco-energy lighting based LEDs†, J. Mater. Chem. C Royal Soc. Chem. https://doi.org/10.1039/c5tc01516b.

[73] Sariga C. Lal, et al., Insights into the structure, photoluminescence and Judd-Ofelt analysis of red emitting SrLaLiTeO6: Eu$^{3+}$ phosphors, J. Alloys Compd. 788 (2019) 1300–1308, https://doi.org/10.1016/j.jallcom.2019.02.260.

[74] Martha Judith Rivera Medina, et al., White emission from ZnS:Eu incorporated in Ac-driven electroluminescent devices via ultrasonic spray pyrolysis, Mater. Chem. Phys. 270 (2021) 124866, https://doi.org/10.1016/j.matchemphys.2021.124866.

[75] Gaofeng Yuan, Photoluminescence evolution and high thermal stability of orange red-emitting Ba$_{3-x}$Sr$_x$ZnNb$_2$O$_9$: Eu$^{3+}$phosphors, J. Solid State Chem. 303 (2021) 122447, https://doi.org/10.1016/j.jssc.2021.122447.

[76] Jan Willem Stouwdam, Lanthanide doped nanoparticles as the active optical medium in polymer based devices, PhD thesis.

[77] G.A. Kumar, M. Pokhrel, D.K. Sardar, Absolute quantum yield measurements in Yb/Ho doped M₂O₂S (M¼Y, Gd, La) upconversion phosphor, Mater. Lett. 98 (2013) 63–66, https://doi.org/10.1016/j.matlet.2013.02.001.

[78] G.L. Bhagyalekshmi, et al., Luminescence dynamics of $Eu^{3+}$ activated and co-activated defect spinel zinc titanate nanophosphor for applications in WLEDs, J. Alloys Compd. 850 (2021) 156660, https://doi.org/10.1016/j.jallcom.2020.156660.

[79] Prasun Mukharjee, Chad M. Shade, Adrienne M. Yingling, Daniel N. Lamont, David H. Waldeck, Stéphane Petoud, Lanthanide sensitization in II–VI semiconductor materials: a case study with terbium (III) and europium (III) in zinc sulfide nanoparticles, J. Phys. Chem. 115 (16) (2011 Apr 28) 4031–4041, https://doi.org/10.1021/jp109786w.

[80] Paula Gorrotxategi, Marianne Consonni, Adrien Gasse, Optical efficiency characterization of LED phosphors using a double integrating sphere system, J. Solid State Lighting 2 (1) (2015), https://doi.org/10.1186/s40539-014-0020-7.